RECEPTIVITY OF A MACH 8 FLOW OVER A SHARP WEDGE TO WALL BLOWING-SUCTION

Xiaowen Wang * **and Xiaolin Zhong** †
University of California, Los Angeles, California 90095

ABSTRACT

In this paper, the receptivity of a Mach 8 flow over a sharp wedge with a half-angle 5.3° to wall blowing-suction disturbances is studied by numerical simulation and linear stability theory (LST). The work is motivated by Fedorov and Khokhlov's[1] theoretical and numerical analysis of the receptivity to wall disturbances of a hypersonic boundary layer over a flat plate. The steady base flow is computed by solving the two-dimensional Navier-Stokes equations with a combination of a fifth-order shock-fitting method and a second-order TVD method. By using the shock-fitting method, the interaction between the blowing-suction disturbances and the oblique shock induced by boundary-layer displacement thickness is taken into account. The characteristics of boundary-layer normal modes are also studied by LST. For unsteady flow simulation, periodic forcing disturbances are introduced to the steady base flow by a blowing-suction actuator on the wedge surface. Based on the results of numerical simulations and LST analysis, the receptivity process of the Mach 8 flow over the sharp wedge to wall blowing-suction disturbances is studied in detail. Specifically, the effects of frequency, location, and lengthscale of the blowing-suction actuator on the receptivity are investigated. It is found that mode S is the dominant boundary-layer normal mode excited by wall blowing-suction disturbances. The numerical results show that mode S is strongly excited only when the blowing-suction actuator is located upstream of the corresponding synchronization point between mode F and mode S. On the other hand, when the blowing-suction actuator is downstream of the corresponding synchronization point, there is a significant decrease of the amplitude of the excited mode S, despite the fact that the blowing-suction actuator is still located in the unstable region of mode S. The results also show that the frequency and lengthscale of the blowing-suction actuator have a significant effect on receptivity of the hypersonic boundary layer to wall blowing-suction.

*Graduate Student Researcher,Mechanical and Aerospace Engineering Department

†Professor, Mechanical and Aerospace Engineering Department,Associate Fellow AIAA.

INTRODUCTION

The performance and control of high-speed space transportation vehicles are significantly affected by the laminar-turbulent transition of supersonic and hypersonic boundary layers, because a turbulent boundary layer generates much higher shear force and heat flux on the surface of the vehicle. Therefore, the accurate prediction of the transition location is critically important for the drag evaluation and aerothermal design of high-speed space transportation vehicles.

In an environment of small initial disturbances, the path to transition over a smooth object generally consists of the following three stages:

- Stage 1: The receptivity process (termed by Morkovin[2]), during which small environmental disturbances enter the boundary layer and excite unstable modes;
- Stage 2: Linear development or growth of boundary-layer unstable modes obtained as the eigen-solutions of the homogeneous linearized stability equations;
- Stage 3: Breakdown to turbulence. After the unstable modes reach certain amplitudes, three-dimensional and non-linear interactions occur in the form of secondary instabilities[3], which eventually leads the boundary layer transition from laminar to turbulent.

For the three-stage transition mechanism, the study of receptivity process is important because it provides initial conditions of amplitude, frequency, and phase angle for boundary-layer normal modes[4]. For supersonic and hypersonic boundary layers, the receptivity process is complex due to the effects of shock wave, compressibility, etc. Theoretically, the governing equations for a receptivity problem are the full Navier-Stokes equations. In 1975, Mack[5] used a linear stability theory which includes the response to incoming acoustic waves. With the extended asymptotic method, Choudhari and Strett[6, 7] investigated the receptivity to localized flow inhomogeneities in a Mach 4.5 boundary layer without considering the effect of the shock wave.

Fedorov and Khokhlov[8] investigated the leading-edge receptivity of supersonic boundary layers to free-stream acoustic waves by an asymptotic method. It was shown that the acoustic waves synchronized with the normal modes of supersonic boundary layers near the leading edge. In their later study[9], two receptivity mechanisms to acoustic waves at the leading edge, diffraction and diffusion, were proposed. More recently, Fedorov and Alexander[10] showed that strong excitations occurred when external waves and wall induced disturbances in resonance with the boundary-layer normal modes. Fedorov and Khokhlov[1] studied the receptivity of a hypersonic boundary layer over a flat plate to wall disturbances using a combination of asymptotic method and numerical simulation. They investigated the receptivity mechanisms to different wall disturbances, i.e., wall vibrations, periodic blowing-suctions, and temperature disturbances. It was found that a strong excitation occurred in local regions where forcing disturbances were resonant with boundary-layer normal modes. They also found that hypersonic boundary layers were more sensitive to blowing-suction disturbances than to wall vibrations and temperature disturbances.

For compressible flow, difficulties arise when the receptivity of supersonic and hypersonic boundary layers is studied experimentally with the help of artificial disturbances. The primary problem is the generation of artificial disturbances, because the lower density in supersonic and hypersonic flows makes it difficult to generate high amplitude disturbances. Therefore, very few experimental studies were carried out to investigate the receptivity of supersonic and hypersonic boundary layers. Kendall[11] experimentally studied the receptivity of supersonic and hypersonic boundary layers to acoustic waves radiated from tunnel walls. The results showed that boundary-layer perturbations grew monotonically immediately downstream of the leading edge. Maslov and Seminov[12] studied the receptivity of a supersonic boundary layer to artificial acoustic waves by utilizing two parallel flat plates. The acoustic waves generated by an electronic discharge system on the lower plate radiated into the external flow and penetrated into the boundary layer of the upper plate as free-stream acoustic disturbances. It was found that the external acoustic waves were converted into boundary-layer oscillations most efficiently at the leading edge, in the neighborhood of the acoustic branch of the neutral curve, and in the vicinity of lower branch of the neutral curve. By using the same experimental technique, Kosinov et al.[13] studied the leading edge receptivity to acoustic waves. The upper plate was placed upside down so that the leading edge appeared as a line acoustic source to the test boundary layer above this plate. Recently, a similar experiment was repeated at a Mach 5.92 flow by Maslov et al.[14] to study the leading edge receptivity of the hypersonic boundary layer. It was found that Tollmien-Schlichting waves are generated by the acoustic waves impinging on the leading edge. They also found that the receptivity coefficients depend on the wave inclination angles.

With the development of powerful super-computers and advanced numerical techniques, numerical simulation of the receptivity by directly solving full Navier-Stokes equations has become feasible. Numerical simulation is easy to control the artificial disturbances by isolating particular disturbances to study the individual effect or by introducing two or more kinds of disturbances to study their combined effects and interactions. Malik et al.[15] studied the receptivity of a hypersonic boundary layer to different external disturbances by solving compressible linearized Navier-Stokes equations. Zhong[16] studied the acoustic receptivity of a hypersonic flow over a parabola by solving full Navier-Stokes equations. It was concluded that the generations of boundary-layer normal modes are mainly due to the interaction of the boundary layer with the transmitted acoustic waves instead of entropy and vorticity waves. In series of papers, Ma and Zhong[17, 18, 19] studied receptivity mechanisms of a supersonic boundary layer to freestream disturbances by a combination of numerical simulation and linear stability theory. It was found that, in addition to the conventional first and second Mack mode, there exist a family of stable modes in the supersonic boundary layer which play an important role in the excitation of unstable Mack modes. For a Mach 10 oxygen flow, receptivity problems were studied in both perfect gas and thermochemically non-equilibrium gas to consider the real gas effect on the receptivity and stability by Ma[20]. Compared with results of perfect gas, the unstable region for non-equilibrium flow is longer and the peak amplitude is higher, which meant that the real gas effect destabilizes the boundary-layer modes. Egorov et al.[21] developed a numerical algorithm and applied it to the numerical simulation of unsteady two-dimensional flow fields relevant to transition at supersonic and hypersonic speeds. An implicit second-order finite-volume technique is used to solve the compressible Navier-Stokes equations. For small forcing amplitudes, the second-mode growth rates predicted by numerical simulation agree well with the growth rates resulted from LST including nonparallel effects. Numerical simulation predicts a nonlinear saturation of fundamental harmonic and rapid growth of higher harmonics.

In addition to the receptivity of flat plates, a Mach 8 flow over a sharp wedge with half-angle 5.3° has also been studied recently. By solving linearized compressible Navier-Stokes equations, Malik et al.[15] investigated the responses of the hypersonic boundary layer to three different types of external forcing: a plane free-stream acoustic wave, a narrow acoustic beam enforced on the oblique shock near the leading edge, and a blowing-suction slot on the wedge surface. They concluded that these three types of forcing eventually re-

sulted in the same boundary-layer instability. However the receptivity mechanism of the hypersonic boundary layer to external disturbances was not studied in detail. Ma and Zhong[22], and Ma[20] studied the receptivity mechanisms of the hypersonic boundary layer to various freestream disturbances, i.e., fast and slow acoustic waves, vorticity waves, and entropy waves, by solving the full Navier-Stokes equations. They found that there exist a family of stable modes in the hypersonic boundary layer in addition to the family of unstable modes. These stable modes play a very important role in the receptivity process. In a previous paper[23], we studied the receptivity of the Mach 8 flow over a sharp wedge with half-angle 5.3° to periodic blowing-suction disturbances. The results showed that the unstable second mode is excited after the synchronization of Mode I and the first mode. The responses of the hypersonic boundary layer to blowing-suction disturbances with different frequencies are quite different. The amplitude of the excited unstable second mode is affected by frequency, location, and profile of the blowing-suction actuator. But the receptivity process of the hypersonic boundary layer to blowing-suction disturbances was not investigated in detail.

Therefore in this paper, the receptivity mechanism of the Mach 8 flow over the sharp wedge to wall blowing-suction is further investigated. Figure 1 shows a schematic of the receptivity of the hypersonic boundary layer over the sharp wedge to wall blowing-suction. After wall blowing-suction is enforced on the wedge surface near the leading edge, boundary-layer normal modes are excited. Simultaneously, the blowing-suction disturbances propagate out of the boundary layer and interact with the oblique shock. Compared with the previous study[23], the simulation domain is extended further downstream in order to obtain more information on receptivity process. In addition, the effects of frequency, location, and lengthscale of the blowing-suction actuator on the receptivity are investigated.

Different terminology on the boundary wave modes have been used in the literatures: Fedorov and Khokhlov[1], Forgoston and Tumin[24], and Ma and Zhong[17]. The 1st mode of Fedorov and Khokhlov has been called Mode I by Ma and Zhong and mode F by Forgoston and Tumin, while the 2nd mode of Fedorov and Khokhlov has been called Mack mode by Ma and Zhong and mode S by Forgoston and Tumin. In order to be consistent with theoretical studies, the terminology "mode S" and "mode F" are used for present study. Mode S represents the Mack mode, while mode F represents the family of stable modes (Mode I, Mode II, etc.) found by Ma and Zhong[22]. Therefore the first Mack mode is mode S before the synchronization point, and the second Mack mode is mode S after the synchronization point. It is found that mode S is the dominant boundary-layer normal mode excited by wall blowing-suction disturbances. The numerical results show that mode S is strongly excited only when the blowing-suction actuator is located upstream of the corresponding synchronization point between mode F and mode S. On the other hand, when the blowing-suction actuator is downstream of the corresponding synchronization point, there is a significant decrease of the amplitude of the excited mode S, despite the fact that the blowing-suction actuator is still located in the unstable region of mode S. The results also show that frequency and lengthscale of the blowing-suction actuator have a significant effect on receptivity of the hypersonic boundary layer to wall blowing-suction.

GOVERNING EQUATIONS AND NUMERICAL METHODS

To simplify the problem, the Mach 8 flow is assumed to be thermally and calorically perfect. In conservative form, the two-dimensional Navier-Stokes equations are written as:

$$\frac{\partial \vec{U}^*}{\partial t^*} + \frac{\partial}{\partial x_1^*}(\vec{F}_{1i}^* + \vec{F}_{1v}^*) + \frac{\partial}{\partial x_2^*}(\vec{F}_{2i}^* + \vec{F}_{2v}^*) = 0 \qquad (1)$$

where the superscript "$*$" represents the dimensional variables. $\vec{U}^*$ is a vector containing the conservative variables of mass, momentum and energy. $\vec{F}_{1i}^*$ and $\vec{F}_{2i}^*$ are inviscid flux vectors, while $\vec{F}_{1v}^*$ and $\vec{F}_{2v}^*$ are viscous flux vectors. Flux vectors can be calculated according to the formula

$$\vec{F}_{ji}^* = \begin{bmatrix} \rho^* u_j^* \\ \rho^* u_1^* u_j^* + p^* \delta_{1j} \\ \rho^* u_2^* u_j^* + p^* \delta_{2j} \\ u_j^*(e^* + p^*) \end{bmatrix} \qquad (2)$$

$$\vec{F}_{jv}^* = \begin{bmatrix} 0 \\ -\tau_{x_1 x_j}^* \\ -\tau_{x_2 x_j}^* \\ -\tau_{x_n x_j}^* u_n^* - k^* \frac{\partial T^*}{\partial x_j^*} \end{bmatrix} \qquad (3)$$

with $j \in \{1, 2\}$, where k^* is the heat conductivity coefficient. For perfect gas, the equation of state and energy are given by

$$p^* = \rho^* R^* T^*, \quad e^* = \rho^* c_v^* T^* + \frac{\rho^*}{2}(u_1^{*2} + u_2^{*2}) \qquad (4)$$

where c_v^* is the specific heat at constant volume. With the assumption that the gas is Newtonian, the viscous stress tensor can be writen as:

$$\tau_{ij}^* = \mu^*(\frac{\partial u_i^*}{\partial x_j^*} + \frac{\partial u_j^*}{\partial x_i^*}) - \frac{2}{3}\mu^* \frac{\partial u_n^*}{\partial x_n^*}\delta_{ij} \qquad (5)$$

for $i \in \{1, 2\}$, $j \in \{1, 2\}$. In numerical simulation, the viscosity coefficient μ^* and the heat conductivity coefficient k^* are calculated using Sutherland's law together with a constant Prandtl number, Pr.

$$\mu^*(T^*) = \mu_r^*(\frac{T^*}{T_r^*})^{3/2}\frac{T_r^* + T_s^*}{T^* + T_s^*} \qquad (6)$$

$$k^*(T^*) = \frac{\mu^*(T^*)c_p^*}{Pr} \tag{7}$$

where $\mu_r^* = 1.7894 \times 10^{-5} N - Sec/m^2$, $T_r^* = 288.0K$, $T_s^* = 110.33K$, c_p^* is the specific heat at constant pressure. In this paper, all the dimensional flow variables are non-dimensionalized by the corresponding free-stream parameters.

A shock-fitting method proposed by Zhong[25, 26] is used to solve the two-dimensional Navier-Stokes equations in the domain bounded by the shock and the wedge surface. The oblique shock is treated as a boundary of the computational domain, which makes it possible for the governing equations to be spatially discretized by high-order finite difference methods. A fifth-order upwind scheme is used to discretize the inviscid flux derivatives. Meanwhile, a sixth-order central scheme is used to discretize the viscous flux derivatives. The Rankine-Hugoniot relation across the shock and a characteristic compatibility relation from behind the shock are combined to solve the flow variables behind the shock. The interaction between the shock and blowing-suction disturbances is solved as a part of solutions. The position and velocity of the shock front are taken as independent flow variables solved by the high-order finite difference method. A three-stage semi-implicit Runge Kutta method derived by Zhong et al.[27, 28] is used for temporal integration. Within a small region near the leading edge, the fifth-order shock-fitting method cannot solve the Navier-Stokes equations accurately because of the singularity at the leading edge. A second-order TVD code of Zhong and Lee[29] is introduced to solve the steady base flow around the leading edge. The TVD solution is then used as the inflow condition to start the solution procedure of the fifth-order shock-fitting method. Details of numerical methods are not presented here, because the same numerical methods as those of Zhong[27] are used in current study.

Due to the symmetric geometry, only the flow field over the upper surface of the sharp wedge is considered in the simulations. Besides the horizontal coordinate x^*, the dimensional distance from the leading edge measured along the wedge surface, s^*, is also used in many plots. With the unit Reynolds number, the dimensional coordinate s^* can be easily converted to non-dimensional local Reynolds number according to the following formula:

$$Re_s = Re_\infty^* \, s^* = 8.2 \times 10^6 s^* \tag{8}$$

In stability studies of boundary layers, the Reynolds number based on the local length scale of boundary-layer thickness, L^*, is generally used:

$$R = \frac{\rho_\infty^* u_\infty^* L^*}{\mu_\infty^*}, \quad L^* = \sqrt{\frac{\mu_\infty^* s^*}{\rho_\infty^* u_\infty^*}} \tag{9}$$

Hence, the relation between R and local Reynolds number Re_s is given by

$$R = \sqrt{Re_s} \tag{10}$$

FLOW CONDITIONS AND BLOWING-SUCTION MODEL

The freestream conditions for currently studied flow over a sharp wedge with half-ange 5.3° are the same as those used by Malik et al[15], Ma and Zhong[22, 20], i.e.,

$$\begin{aligned} &M_\infty = 8.0\,, && T_\infty^* = 54.78K\,, \\ &p_\infty^* = 389Pa\,, && Pr = 0.72\,, \\ &Re_\infty^* = \rho_\infty^* u_\infty^* / \mu_\infty^* = 8.2 \times 10^6/m\,, \end{aligned}$$

For viscous flow, the physical boundary conditions on the wedge surface are non-slip velocity condition and isothermal or adiabatic temperature condition. For the simulation of steady base flow, adiabatic temperature condition is used. When blowing-suction disturbances are enforced to the steady base flow, the isothermal temperature condition, which is a standard boundary condition for theoretical and numerical studies for high frequency disturbances, is used for unsteady flow. For present study, inlet conditions are specified. Details of the inlet condition will be further discussed later. High-order extrapolation is used for outlet conditions because the flow is hypersonic at the exit boundary except there is a small region near the wedge surface where flow is subsonic.

In Fedorov and Khokhlov's[1] theoretical and numerical analysis of boundary-layer receptivity to wall disturbances, the wall blowing-suction disturbance has the following traveling-wave form:

$$\begin{bmatrix} u' \\ v' \\ w' \\ \theta' \end{bmatrix} = g(x) \begin{bmatrix} 0 \\ 1 \\ 0 \\ 0 \end{bmatrix} \exp(i\alpha_c x + i\beta_c z - i\omega t) \tag{11}$$

where u',v',w' are velocity disturbances in stream-wise, wall-normal, and span-wise directions respectively, while θ' is the temperature disturbance. α_c and β_c are the components of the disturbance wave number in stream-wise and span-wise directions. ω is the circular frequency. g(x) represents the disturbance shape of the blowing-suction actuator. Equation (11) implies that wall blowing-suction is only related to the wall-normal velocity disturbance. For this model, instantaneous mass flux is introduced to the boundary layer even if g(x) is an anti-symmetric function, because the density is not a constant within the blowing-suction actuator.

Another model for blowing-suction disturbances is to use the mass flux oscillation on the wall, which has been used by Eiβler and Bestek[30], and Egorov et al.[21]. The blowing-suction disturbance is as follows:

$$q_w(x,t) = \frac{\rho_w v_w}{\rho_\infty U_\infty} = A \sin(2\pi \frac{x - x_1}{x_2 - x_1}) \sin(\omega t) \tag{12}$$

where A is the amplitude of mass flux oscillation, ρ_w and v_w are the density and wall-normal velocity on the wall, ρ_∞ and U_∞ are the density and stream-wise velocity in freestream, x_1, x_2 are boundaries of the blowing-suction actuator. For this model, the net mass flux introduced to the boundary layer is zero at any instant.

In present study, a blowing-suction model similar to Eq. (12) is used. With this model, the mass flux oscillation within the blowing-suction actuator on the wedge surface can be written as:

$$(\rho^* v^*)' = \rho_0^* \epsilon \beta(l) \sum_{n=1}^{N} \sin(\omega_n^* t^*) \tag{13}$$

where ρ_0^* is a local constant depending on the location of the blowing-suction actuator, ϵ is a small non-dimensional parameter representing the amplitude of the blowing-suction disturbance. $\beta(l)$ is the shape function defined as

$$\begin{cases} \beta(l) = 20.25l^5 - 35.4375l^4 + 15.1875l^2 \\ \qquad \text{if } \ l <= 1 \\ \beta(l) = -20.25(2-l)^5 + 35.4375(2-l)^4 \\ \qquad -15.1875(2-l)^2 \ \text{ if } \ l >= 1 \end{cases} \tag{14}$$

The variable l is a non-dimensional coordinate defined on the blowing-suction actuator,

$$l = 2(s^* - s_i^*)/(s_e^* - s_i^*) \tag{15}$$

where s_i^*, s_e^* are the boundaries of the blowing-suction actuator. The net mass flux introduced to the boundary layer by this model is zero at any instant. The specific 5th-order-polynomial shape function makes the mass flux oscillation smooth at the boundaries of the blowing-suction actuator. In Eq. (13), ω_n^* are the circular frequencies of multi-frequency blowing-suction disturbances:

$$\omega_n^* = 2\pi f_n^* \tag{16}$$

The circular frequency is non-dimensionalized according to

$$\omega_n = \frac{\omega_n^* L^*}{U_\infty^*} \tag{17}$$

The frequency f_n^* is non-dimensionalized as:

$$F_n = \frac{2\pi f_n^* \mu_\infty^*}{\rho_\infty^* U_\infty^{*2}} = \frac{\omega_n^* \mu_\infty^*}{\rho_\infty^* U_\infty^{*2}} \tag{18}$$

With the definitions of Reynolds number R and the non-dimensional frequency F_n, the non-dimensional circular frequency can also be expressed as

$$\omega_n = RF_n \tag{19}$$

In simulations, the amplitude of blowing-suction disturbance is chosen so that it is at least one order of magnitude larger than the maximum numerical noise, while it is small enough to preserve the linear properties of the disturbances. The specific amplitude coefficient ϵ used in the current study is:

$$\epsilon = 1.0 \times 10^{-5} \tag{20}$$

Table 1: Frequency, circular frequency, and non-dimensional frequency for the multi-frequency blowing-suction disturbances

n	$f_n^*(kHz)$	$\omega_n^*(kHz)$	$F_n \times 10^6$
1	14.92	93.74	9.63
2	29.84	187.48	19.26
3	44.76	281.23	28.89
4	59.68	374.97	38.52
5	74.60	468.71	48.15
6	89.52	562.45	57.78
7	104.44	656.19	67.41
8	119.36	749.94	77.04
9	134.28	843.68	86.67
10	149.20	937.42	96.30
11	164.12	1031.16	105.93
12	179.04	1124.91	115.56
13	193.96	1218.65	125.19
14	208.88	1312.39	134.82
15	223.80	1406.13	144.45

The frequency, circular frequency, and non-dimensional frequency for blowing-suction disturbances are listed in Table 1.

RESULTS AND DISCUSSIONS

Steady State Solution

The steady base flow is calculated by the combination of a fifth-order shock-fitting method and a second-order TVD method. For the fifth-order shock-fitting method, the computational domain begins at $s^* = 0.00409m$, and ends at $s^* = 1.48784m$. In terms of R, the full domain spans from $R = 183.1$ to $R = 3485.4$. In actual simulations, the computational domain is divided into 30 zones with a total of 5936 grid points in stream-wise direction and 121 grid points in wall-normal direction. 41 points are used in the buffering regions between two neighboring zones, which is proved to be sufficient to make the solution accurate and smooth within the whole domain. An exponential stretching function is used in the wall-normal direction to cluster more points inside the boundary layer. On the other hand, the grid points are uniformly distributed in stream-wise direction. The accuracy of the results based on this grid structure has been evaluated by grid refinement studies to ensure the grid independence of the numerical solutions.

For the first zone, the inlet conditions are obtained from the results of the second-order TVD shock-capturing method. For other zones, inlet conditions are

interpolated from the results of previous zone. Figure 2 compares the density contours of steady flow solutions obtained from the second-order TVD method and the fifth-order shock-fitting method. It shows that density contours have an excellent agreement within the buffering region, which indicates that the TVD solutions are accurate enough to be used as inlet conditions for the numerical simulation with the fifth-order shock-fitting method. The combination of the shock-fitting method and the TVD method has also been validated in cases of supersonic and hypersonic steady flows over a flat plate by Ma and Zhong[31].

Figure 3 shows the pressure contours of the steady base flow solved by the fifth-order shock-fitting method. A part of the pressure field from $x^* = 0.05$ m to $x^* = 0.15$ m is amplified to show clearly the pressure contour within the boundary layer. The upper boundary of the flow field represents the oblique shock. Apparently, pressure is almost a constant across the boundary layer and along the Mach lines, which is consistent with the boundary-layer theory and supersonic aerodynamics. Figure 4 compares the pressure distribution along the wedge surface of numerical simulation result with that of the theoretical inviscid solution. Near the leading edge, there exists great pressure gradient for numerical result, which is the result of the strong interaction between the oblique shock and the viscous boundary layer. From upstream to downstream, such an interaction becomes weaker and weaker with the oblique shock moves away from the boundary layer. Therefore the pressure gradient decreases, and the pressure tends to a constant. However the pressure of numerical simulation at the exit of computational domain is still greater than that of the theoretical inviscid solution due to the interaction between the inviscid external flow and the viscous boundary layer. The shock front position and the distribution of shock angle of numerical result are compared with those of the theoretical inviscid solution respectively in Fig. 5. The differences between the numerical result and the inviscid solution indicate that the shock front of numerical simulation result is not a straight line with the shock angle decreasing from 14.793° near the leading edge to 11.307° at the exit of the computational domain. Figure 6 compares the distribution of Mach number behind the shock of numerical result with that of the theoretical inviscid solution. It shows that Mach number of numerical simulation result increases from 5.911 near leading edge to 6.746 at the exit of the computational domain. For inviscid Mach 8 flow over the sharp wedge, the theoretical shock angle and Mach number behind the shock are 11.102° and 6.798 respectively. Therefore, the shock angle and Mach number behind the shock of numerical simulation result approach corresponding values of the inviscid theoretical solution downstream where the oblique shock moves far away from the boundary layer and the interaction between the oblique shock and the viscous boundary layer becomes negligible. However, the shock angle and Mach number behind the shock of numerical simulation result cannot be equal to corresponding values of the inviscid theoretical solution because of the interaction between the inviscid external flow and the viscous boundary layer.

Characteristics of Boundary-Layer Normal Modes

The characteristics of boundary-layer normal modes of the Mach 8 flow over the sharp wedge with half-angle 5.3° is studied by the linear stability theory (LST). In the LST analysis, the steady base flow can be either from numerical simulation or from the self-similar boundary-layer solution. Although the numerical simulation result is more accurate and efficient for LST analysis at one location, it is inconvenient for LST analysis at series of locations. Because the numerical result is not self-similar, it must be totally updated when the LST analysis is applied to a different location. Therefore the self-similar boundary-layer solution is used to investigate the general characteristics of the boundary-layer normal modes.

For the LST analysis, the characteristics of steady base flow is of great importance. Figure 7 compares the stream-wise velocity and its first-order derivative of numerical simulation with those of the self-similar boundary-layer solution at $s^* = 0.62784$ m, corresponding to $R = 2264.13$. While the second-order derivative of stream-wise velocity at the same location of numerical simulation result is compared with that of the self-similar boundary-layer solution in Fig. 8. Figure 9 compares the temperature and its first-order derivative of numerical simulation result with those of the self-similar boundary-layer solution at $s^* = 0.62784$ m. All these figures show that the results of the self-similar boundary-layer solution and the numerical simulation agree well except the small difference in the second-order derivative of stream-wise velocity. It was found in Ma and Zhong[17] that the linear stability characteristics based on self-similar boundary-layer solution are close to those based on numerical simulation result, although shock/boundary layer interaction and flow compressibility are neglected in the self-simliar boundary-layer solution.

Eigenvalue spectra of boundary-layer normal modes for the disturbance with the non-dimensional frequency $F_6 = 57.78 \times 10^{-6}$ ($f_6^* = 89.52$ kHz) at the location $R = 1980.44$ ($s^* = 0.48036$ m) are plotted in Fig. 10, where α_r and α_i are the real and imaginary parts of the wave number. It shows that there exist three continuous modes corresponding to the fast acoustic mode, the vorticity or entropy mode, and the slow acoustic mode. The figure also shows that there exist discrete modes corresponding to boundary-layer normal modes. Two discrete modes are outlighted by circles in the figure. Investigation of the corresponding eigenfunctions indi-

cates: one is mode S, and the other is mode F. Mode F is a stable mode called Mode I by Ma and Zhong [17, 18]. Mode F starts from the continuous modes on the left side of the figure and passes the continuous modes in the middle as ω increases.

Figure 11 compares the non-dimensional phase velocities of boundary-layer normal modes at three frequencies $F_5 = 48.15 \times 10^{-6}$ ($f_5^* = 74.60$ kHz), $F_6 = 57.78 \times 10^{-6}$ ($f_6^* = 89.52$ kHz), and $F_7 = 67.41 \times 10^{-6}$ ($f_7^* = 104.44$ kHz) as a function of the non-dimensional circular frequency, ω. The three dashed lines represent the non-dimensional phase velocities of fast acoustic mode ($a/U_\infty = 1 + M_\infty^{-1}$), vorticity or entropy mode ($a/U_\infty = 1$), and slow acoustic mode ($a/U_\infty = 1 - M_\infty^{-1}$) respectively. The excellent agreement of the phase velocities of different frequencies indicate that the phase velocity is a function of ω. In Fig. 11, mode F originates from the fast acoustic mode and passes the vorticity or entropy mode as shown in Fig. 10, while mode S originates from the slow acoustic mode. The figure also shows that mode S synchronizes with mode F at $\omega_s = 0.11443$, $(a/U_\infty)_s = 0.93349$. At the synchronization point, the non-dimensional phase velocities of mode S and mode F are the same, and their eigenfunctions have very similar profile as shown in Fig. 12. The position of the synchronization point has a constant value of ω_s (= 0.11443). However in s^* coordinate, the positions of the synchronization point are different for different frequencies, which can be calculated using

$$s_{sn}^* = \frac{(\omega_s/F_n)^2}{Re_\infty} \tag{21}$$

with s_{sn}^*, the position of the synchronization point in R coordinate, R_{sn}, can be calculated according to Eqs. (10) and (8).

Comparisons of the non-dimensional wave number α_r and growth rate α_i for mode F and mode S at the same three frequencies are shown in Figs. 13 and 14 respectively. Figure 13 shows that the non-dimensional wave numbers of boundary-layer modes does not depend on dimensional frequency. In stead, it is a function of ω only. In Fig. 14, the vertical dashed line represents the position of the synchronization point, while the horizontal dashdot line stands for the neutral modes ($\alpha_i = 0$). It shows the growth rates of both mode S and mode F are almost independent of dimensional frequency. Mode S is unstable from $\omega_I = 0.04$ to $\omega_{II} = 0.23$, while mode F is always stable. The Branch II neutral point of mode S, ω_{II}, is approximately independent of the dimensional frequency. In s^* coordinate, the positions of the Branch II neutral point change with different frequencies, which can be calculated using

$$s_{IIn}^* = \frac{(\omega_{II}/F_n)^2}{Re_\infty} \tag{22}$$

Table 2 provides coordinates of the synchronization point (s_{sn}^*, R_{sn}) and the Branch II neutral point (s_{IIn}^*) for the multi-frequency blowing-suction disturbances.

Table 2: Coordinates of the synchronization point and the Branch II neutral point for blowing-suction disturbances

n	s_{sn}^* (m)	R_{sn}	s_{IIn}^* (m)
1	16.9885	11882.658	68.38297
2	4.2471	5941.329	17.09574
3	1.8876	3960.886	7.59811
4	1.0618	2970.664	4.27394
5	0.6795	2376.532	2.73532
6	0.4719	1980.443	1.89953
7	0.3467	1697.523	1.39557
8	0.2654	1485.332	1.06848
9	0.2097	1320.295	0.84423
10	0.1699	1188.266	0.68383
11	0.1404	1080.242	0.56515
12	0.1180	990.222	0.47488
13	0.1005	914.051	0.40463
14	0.0867	848.761	0.34889
15	0.0755	792.177	0.30392

Receptivity to the Blowing-Suction Actuator at A Single Frequency

According to our previous study[23], the receptivity of the hypersonic boundary layer to wall blowing-suction is affected by frequency, location, and shape function of the blowing-suction actuator. We first study the receptivity process for the case of a blowing-suction actuator with a single frequency. The blowing-suction disturbance with the single frequency $f_5^* = 74.60$ kHz ($F_5 = 48.15 \times 10^{-6}$) is introduced with the blowing-suction actuator on the wedge surface from $s_i^* = 0.10184$ m to $s_e^* = 0.11384$ m (corresponding to R from 911.88 to 964.10) to investigate the receptivity process. For this specific case, the blowing-suction disturbance is in the following form:

$$(\rho^* v^*)' = \rho_0^* \epsilon \beta(l) \sin(\omega_5^* t^*) \tag{23}$$

where ρ_0^* is the multiplication of steady base flow density and wall-normal velocity after the shock at s_i^* location. The effect of different blowing-suction models is first evaluated. The first model is given by Eq. (23). The second model is to set wall-normal velocity disturbance, $v^{*\prime}$, only, i.e.,

$$v^{*\prime} = v_0^* \epsilon \beta(l) \sin(\omega_5^* t^*) \tag{24}$$

where v_0^* is the wall-normal velocity after the shock at s_i^* location. In Eq. (23), the constant ρ_0^* is chosen so that the wall-normal velocity disturbances induced by the two blowing-suction models have the same scale. The wall-normal velocity disturbance introduces instantaneous mass flux to the boundary layer, which is shown in Fig. 15 for one period of the base frequency $f_1^* = 14.92$ kHz. It shows that the instantaneous mass flux is pe-

riodic and the dimensional amplitude of the flux oscillation is very small. During one period of the base frequency, the net mass flux introduced to the boundary layer is nearly zero because of the sine-like profile.

Figure 16 compares non-dimensional amplitudes of the pressure perturbation along the wedge surface for the two blowing-suction models given by Eqs. (23) and (24). The good agreement between the amplitudes indicates that the effect of the small instantaneous mass flux oscillation on receptivity is negligible, and the two blowing-suction models are equivalent under the given conditions. In order to show clearly the small structures, comparison of amplitudes of the upstream pressure perturbation along the wedge surface for the two blowing-suction models is redrawn in Fig. 17. Again, there is a good agreement between the amplitudes of pressure perturbation. Furthermore, there are strong modulations just downstream of the blowing-suction actuator. After $s^* \approx 0.6$ m, the amplitude of pressure perturbation increases monotonically. Figure 18 shows the distribution of non-dimensional instantaneous pressure perturbation along the wedge surface. The amplification of the pressure perturbation from upstream to downstream indicates an unstable mode is excited inside the boundary layer.

To check the properties of the unstable mode, fast Fourier transformation (FFT) is applied to the non-dimensional instantaneous pressure perturbation along the wedge surface, which leads to

$$p'(s^*,t) = \Sigma |p'_n(s^*)| e^{i[\phi'_n(s^*) - \omega^*_n t^*]} \tag{25}$$

where $p'(s^*,t)$ represents the non-dimensional instantaneous pressure perturbation along the wedge surface. $|p'_n(s^*)|$ and $\phi'_n(s^*)$ are real variables representing the perturbation amplitude and phase angle respectively, from which a local wave number α_{rn} and a local growth rate α_{in} of the perturbation with the frequency f^*_n can be calculated by

$$\alpha_{rn} = \frac{d\phi'_n}{ds^*}, \quad \alpha_{in} = -\frac{1}{|p'_n|}\frac{d|p'_n|}{ds^*} \tag{26}$$

Figures 19, 20, and 21 compares the wave number α_r, the growth rate α_i, and the non-dimensional phase velocity a/u_∞ for the unstable mode obtained by the numerical simulation with the corresponding values of mode F and mode S computed by LST. These figures are for the frequency f^*_5. It is shown that the wave number, growth rate, and the non-dimensional phase velocity of the unstable mode fit well with the properties of mode S after $\omega = 0.095$ ($s^* = 0.477$ m), which indicates that the unstable mode excited by the blowing-suction actuator is mode S. In Fig. 20, it is also noticed that mode S obtained by numerical simulation becomes stable much earlier than LST result. In other words, the Branch II neutral point of mode S moves upstream compared with the LST result.

Figures 25 and 26 compare the eigenfunctions of mode F and mode S with the instantaneous pressure perturbation (frequency f^*_5) from numerical simulation at eight different locations. Figure 25 shows that the pressure perturbation of the simulation solution is much closer to the eigenfunction of mode S, which indicates that mode S is the dominant mode inside the local boundary layer. The existence of mode F is possible, but it will decay downstream because mode F is inherent stable. Figure 26 shows that there are good agreements between the eigenfunction of mode S and the instantaneous pressure perturbation from numerical simulation. These agreements also indicate that the unstable mode excited by the blowing-suction actuator is mode S. Therefore mode S is the dominant boundary-layer mode excited by the blowing-suction actuator.

Effect of Frequency of the Blowing-Suction Actuator

In preceding section, the receptivity of the hypersonic boundary layer to the blowing-suction actuator with the single frequency of $f^*_5 = 74.60$ kHz ($F_5 = 48.15 \times 10^{-6}$) was studied. The results show that mode S is the dominant boundary-layer normal mode excited by the blowing-suction actuator. The effect of disturbance frequency on the receptivity to wall blowing-suction is studied by introducing multi-frequency blowing-suction disturbances to the boundary layer. Blowing-suction disturbances with fifteen frequencies (f^*_n listed in Table 1 with n from 1 to 15) are imposed with a blowing-suction actuator on the wedge surface from $s^*_i = 0.05184$ m to $s^*_e = 0.06384$ m (corresponding to R from 650.59 to 721.98). The blowing-suction disturbances are related to the mass flux oscillations according to Eq. (13), and the shape function of the blowing-suction actuator is given by Eq. (14).

Figure 22 shows the distribution of instantaneous pressure perturbation along the wedge surface. Due to the modulation between the multiple frequencies, the instantaneous pressure perturbation has multiple peaks from upstream to downstream. The amplification of the perturbation from upstream to downstream indicates the existence of the unstable mode S. In order to investigate the effect of disturbance frequency on the receptivity, fast Fourier transformation (FFT) is applied to decompose the instantaneous pressure perturbation. Figure 27 compares pressure perturbation amplitudes along the wedge surface with different frequencies. Although the initial amplitudes of blowing-suction disturbances with different frequencies are the same, the behaviors of pressure perturbations are quite different. As shown in Fig. 27 (a), the perturbations with frequencies f^*_1, f^*_2, and f^*_3 modulate after the blowing-suction actuator and grow slowly from upstream to downstream, which implies that mode S is excited. In Figs. 27 (b) and 27 (c), the perturbations with frequencies f^*_n (n from 4 to 11) grow fast after the blowing-suction actuator, which indicates that mode S is excited by blowing-suction disurbances with these frequencies and becomes

more unstable after the synchronization point. Pressure perturbations with higher frequencies shown in Fig. 27 (d) increase in a very small region after the blowing-suction actuator. The visible oscillations in perturbation amplitudes downstream with $s^* > 0.2$ m are resulted from the effect of harmonics.

For each frequency in Figs. 27 (b) to (d), the synchronization point can be obtained from Table 2. Figure 27 show that the perturbation amplitudes start to grow substantially only in the region after the synchronization point for each frequency. However the perturbations with frequencies f_n^* $(n > 4)$ decrease far before reaching to the corresponding Branch II neutral point. Comparison of numerical simulation growth rates and LST growth rates with the frequencies f_5^*, f_6^*, and f_7^* is shown in Fig. 23. The numerical simulation growth rates have a good agreement with the LST results from $\omega = 0.11$ to $\omega = 0.13$. On the other hand, the difference in Branch II neutral points of numerical simulation and LST may be caused by the approximations in LST, because the effects of the nonparallel boundary-layer flow, the pressure gradient, and the oblique shock are left out in LST. To show the positions on wedge surface where mode S becomes unstable for different frequencie, Figure 24 plots α_i as a function of s^* for the same set of frequencies as that in Fig. 23. With increasing frequency, the synchronization point moves upstream, i.e., mode S becomes unstable earlier.

Comparisons of DNS wave numbers of perturbations with frequencies f_n^* $(n > 3)$ with the LST wave number are shown in Fig. 28. The good agreement of numerical wave numbers and the LST result downstream shows that mode S is excited by wall blowing-suction with these frequencies. Figure 28 also shows that the synchronization point is a function of ω. In s^* coordinate, the position where mode S becomes unstable moves upstream with increasing frequency, which is clearly shown in Figs. 27 (b), 27 (c), and 27 (d). The perturbations with frequencies f_n^* (n from 1 to 3) start to increase slowly at a position upstream to the corresponding synchronization point, because mode S is slightly unstable before the synchronization point. The synchronization point for perturbations with these three frequencies is further downstream to the computational domain currently considered.

Effect of Location of the Blowing-Suction Actuator

In order to investigate the effect of location of the blowing-suction actuator on receptivity, a series of independent simulations have been carried out for blowing-suction actuators at different locations on the wedge surface. In each case, wall blowing-suction with fifteen frequencies (f_n^* listed in Table 1 with n from 1 to 15) is superimposed on the wedge surface. For all simulations, the blowing-suction disturbances are related to the mass flux oscillation according to Eq. (13). The shape function of the blowing-suction actuator is given by Eq. (14). However, the constant ρ_0^* in Eq. (13) and the location of the blowing-suction actuator (s_i^* and s_e^* in Eq. (15)) are different for the independent cases. In present study, location of the blowing-suction actuator is defined as

$$s_c^* = \frac{s_i^* + s_e^*}{2} \tag{27}$$

with s_c^*, location of the blowing-suction actuator in R coordinate, R_{sc}, can be calculated according to Eqs. (10) and (8). Specifically, ρ_0^* constant and locations of the blowing-suction actuator of the seven cases investigated in this paper are listed in Table 3, where ρ_0^* is the multiplication of steady base flow density and wall-normal velocity after the shock at s_i^* location with the dimension kg/(m$^2 s$).

Table 3: Constant ρ_0^* and locations of blowing-suction actuator for the seven cases by which the effect of location of blowing-suction actuator on receptivity is investigated

case	ρ_0^*	s_i^* (m)	s_e^* (m)	s_c^* (m)	R_{sc}
1	0.2141	0.05184	0.06384	0.05784	687.2
2	0.1252	0.10184	0.11384	0.10784	938.4
3	0.0961	0.15184	0.16384	0.15784	1135.2
4	0.0807	0.20184	0.21384	0.20784	1302.7
5	0.0708	0.25184	0.26384	0.25784	1450.9
6	0.0637	0.30184	0.31384	0.30784	1585.4
7	0.0545	0.40184	0.41384	0.40784	1824.8

As shown in Fig. 11, the synchronization point of mode F and mode S has a non-dimensional circular frequency of $\omega_s = 0.11443$ and a non-dimensional phase velocity of $(a/U_\infty)_s = 0.93349$. Although the synchronization point in ω coordinate does not depend on the dimensional frequency, its location in s^* and R coordinates is different for different dimensional frequency. The synchronization points in s^* and R coordinates for the 15 frequencies investigated in present study are calculated with Eqs. (21) and (10), which are tabulated in Table 2 as s_{sn}^* and R_{sn}.

Table 2 shows that the synchronization point moves upstream with the frequency of disturbance increasing. Therefore, the blowing-suction actuator may be located either before or after the synchronization point when it moves downstream from case 1 to case 7. Table 4 lists location of the blowing-suction actuator with respect to the synchronization point for the seven cases. "$s_c^* < s_{sn}^*$" represents that the blowing-suction actuator is located upstream of the corresponding synchronization point, while "$s_c^* < s_{sn}^*$" represents that the blowing-suction actuator is downstream of the corresponding synchronization point.

For example, for the frequency $f_5^* = 74.60$ kHz, lo-

Table 4: Location of the blowing-suction actuator with respect to the synchronization point for the seven cases by which the effect of location of the blowing-suction actuator on receptivity is investigated

case	frequency: $s_c^* < s_{sn}^*$	frequency: $s_c^* > s_{sn}^*$
1	n from 1 to 15	none
2	n from 1 to 12	n from 13 to 15
3	n from 1 to 10	n from 11 to 15
4	n from 1 to 9	n from 10 to 15
5	n from 1 to 8	n from 9 to 15
6	n from 1 to 7	n from 8 to 15
7	n from 1 to 6	n from 7 to 15

cations of the blowing-suction actuator in all cases are upstream to the corresponding synchronization point. While for the frequency $f_{10}^* = 149.20$ kHz, ocations of the blowing-suction actuator in cases from 1 to 3 are upstream to the corresponding synchronization point, while locations of the blowing-suction actuator in other cases are downstream of the corresponding synchronization point.

To show the effect of location of the blowing-suction actuator on receptivity, the perturbations of the same frequency for the seven cases are plotted together. Figures 29, 30, and 31 compare the pressure perturbation amplitudes with a same frequency for the seven cases of different blowing-suction locations on the wedge surface. In these figures, the numbers within the small rectangular represent the different cases. For the frequency $f_4^* = 59.68$ kHz, the blowing-suction actuator in all seven cases is located upstream of the corresponding synchronization point at $s_{s4}^* = 1.0618$ m. Figure 29 (a) shows that mode S is strongly excited for all seven cases. Furthermore, the amplitudes of pressure perturbations developed in the boundary layer decrease dramatically when the blowing-suction actuator moves from upstream to downstream. Figures 29 (b) and 29 (c) show similar results for the frequencies $f_5^* = 74.60$ kHz and $f_6^* = 89.52$ kHz respectively. When the frequency is $f_7^* = 104.44$ kHz, location of the blowing-suction actuator is upstream of the corresponding synchronization point at $s_{s7}^* = 0.3467$ m in cases from 1 to 6, however it is downstream of the corresponding synchronization point in case 7. Figure 29 (d) shows that mode S is apparently excited for cases from 1 to 6. When the blowing-suction actuator is located downstream of the corresponding synchronization point in case 7, there is a significant decrease of the amplitude of the excited mode S, despite the fact that the blowing-suction actuator is still located in the unstable region of mode S. For the frequency $f_8^* = 119.36$ kHz, Figure 30 (a) shows that mode S is strongly excited for cases from 1 to 5, while there is a significant decrease of the amplitude of the excited mode S for case 6 and case 7. Because locations of blowing-suction actuator in cases from 1 to 5 are upstream of the corresponding synchronization point at $s_{s8}^* = 0.2654$ m, however the blowing-suction actuator is located downstream of the corresponding synchronization point in case 6 and case 7. Again, the blowing-suction actuator is still located in the unstable region of mode S. When the frequency changes to $f_9^* = 134.28$ kHz, the blowing-suction actuators are located upstream of the corresponding synchronization point at $s_{s9}^* = 0.2097$ m in cases from 1 to 4, however locations of the blowing-suction actuator in cases from 5 to 7 are downstream of the corresponding synchronization point. Figure 30 (b) shows that mode S is strongly excited for cases from 1 to 4, while the excited mode S decrease dramatically for cases from 5 to 7. For the frequencies f_n^* with n from 10 to 15, similar conclusion can be drawn. In Fig. 31, the visible modulation and growth of pressure perturbations downstream with $s^* > 0.2$ m are resulted from harmonics.

For quantitative analysis, the response coefficients of pressure perturbations with a same frequency for the seven cases are compared in Fig. 32. In the figure, $(p\prime/p_\infty)_{mx}$ represents the maximum amplitude of pressure perturbation along the wedge surface excited by the blowing-suction actuator, while $(p\prime/p_\infty)_{in}$ represents the initial amplitude of pressure perturbation along the wedge surface introduced by the blowing-suction actuator. The ratio of $(p\prime/p_\infty)_{mx}$ and $(p\prime/p_\infty)_{in}$ is defined as the response coefficient. The horizontal coordinate, $R_{sc} - R_{sn}$, is the signed distance between the blowing-suction actuator and the synchronization point. The negative horizontal coordinate means that the blowing-suction actuator is upstream of the synchronization point, while the positive horizontal coordinate means that the blowing-suction actuator is located downstream of the synchronization point. The vertical dashdot line represents a special case in which the blowing-suction actuator and the synchroniztion point are overlaped. Fig. 32 (a) shows clearly that response coefficient for the same frequency decreases dramatically with the blowing-suction actuator approaching the synchronization point. The high response coefficients indicate that mode S is strongly excited, because locations of the blowing-suction actuator in all cases are upstream of the corresponding synchronization points for frequencies f_4^*, f_5^*, and f_6^*. For frequencies f_n^* with n from 7 to 9, Fig. 32 (b) shows that response coefficient for the same frequency generally decreases with $R_{sc} - R_{sn}$ increasing except for the jump near $R_{sc} - R_{sn} = -200$. It is found that the response coefficients are much smaller when $R_{sc} - R_{sn}$ is positive. This indicates that the excited mode S is much weaker when the blowing-suction actuator is downstream of the synchronization point, despite the fact that the blowing-suction actuator is still located in the unstable region of mode S. Figures 32 (c) and 32 (d) also show that the response coefficients for negative $R_{sc} - R_{sn}$ is higher than

those for positive $R_{sc}-R_{sn}$ when the frequency is fixed, because mode S is strongly excited in the cases with negative $R_{sc}-R_{sn}$ which is clearly shown in Figs. 29 (d), 30 and 31. Different from Fig. 32 (a), the response coefficients in Figs. 32 (c) and 32 (d) for $R_{sc}-R_{sn}>300$ increase slowly with $R_{sc}-R_{sn}$ increasing.

To summarize, the simulation results indicate that the synchronization point plays an important role in the excitation of mode S by the blowing-suction actuator. Mode S is strongly excited when the blowing-suction actuator is located upstream of the corresponding synchronization point. On the other hand, when the blowing-suction actuator is downstream of the corresponding synchronization point, there is a significant decrease of the amplitude of the excited mode S. This decrease happens even when the blowing-suction actuator is still inside the unstable region of mode S. Again, this suggest that the synchronization point is critical to the receptivity process. The relationship between the location of blowing-suction actuator and the synchronization point indicates: in order to control or delay the laminar-turbulent transition more efficiently, the blowing-suction actuator should be located upstream of the synchronization point of mode S and mode F.

Effect of Lengthscale of the Blowing-Suction Actuator

In this section, the effect of lengthscale of the blowing-suction actuator on receptivity is studied. A series of independent simulations are carried out for the receptivity investigation of the hypersonic boundary layer to multi-frequency disturbances enforced by blowing-suction actuators with different lengthcales at the same location (corresponding to case 7 in Table 3). Wall blowing-suction with fifteen frequencies (f_n^* listed in Table 1 with n from 1 to 15) is superimposed with the blowing-suction actuator. Similarly, the blowing-suction disturbances are related to the mass flux oscillation according to Eq. (13), and the shape function of the blowing-suction actuator is given by Eq. (14). However the lengthscale of the blowing-suction actuator is different for independent cases. Specifically, lengthscales of the blowing-suction actuator of the eight cases are investigated in this paper. Table 5 lists the lengthscale of the blowing-suction actuator, which is non-dimensinalized by that of case 2.

Figure 33 compares pressure perturbation amplitudes along the wedge surface with different frequencies for case 2. It is clearly shown in the figure that the behaviors of pressure perturbations with different frequencies are quite different although the initial amplitudes are the same. As shown in Fig. 33 (a), amplitudes of pressure perturbations with frequencies f_1^*, f_2^*, and f_3^* modulation after the blowing-suction actuator and grow up slowly from upstream to downstream. In Fig. 33 (b) the perturbations with frequencies f_n^* (n from 4 to 6) grow fast after the blowing-suction actuator, which indicates

Table 5: Lengthscales of the blowing-suction actuator for the eight cases by which the effect of lengthscale of blowing-suction actuator on receptivity is investigated

case	s_i^* (m)	s_e^* (m)	$s_e^*-s_i^*$ (m)	lengthscale
1	0.40359	0.41184	0.00825	0.6875
2	0.40184	0.41384	0.01200	1.0000
3	0.40059	0.41484	0.01425	1.1875
4	0.39984	0.41559	0.01575	1.3125
5	0.39934	0.41609	0.01675	1.3958
6	0.39809	0.41734	0.01925	1.6042
7	0.39584	0.41984	0.02400	2.0000
8	0.39084	0.42459	0.03375	2.8125

that mode S is strongly excited by blowing-suction disturbances with these frequencies. However the pressure perturbation with the frequency f_7^* is much weaker. As discussed in preceding section, the blowing-suction actuator is downstream of the synchronization point for the frequency f_7^*. Therefore, the excited mode S is much weaker. Similarly, pressure perturbations with higher frequencies as shown in Figs. 33 (c) and 33 (d) only have small amplitudes.

To investigate the effect of lengthscale of the blowing-suction actuator on receptivity, the perturbations with the same frequency for the eight cases are plotted together. Figures 34 compares pressure perturbation amplitudes with the same frequency f_4^* and f_6^* for the eight cases that wall disturbances are introduced by the blowing-suction actuators with different lengthscale at the same location on the wedge surface. For the frequency $f_4^*=59.68$ kHz, Figure 34 (a) shows that mode S is strongly excited for all eight cases, because blowing-suction actuators in all the cases are located upstream of the corresponding synchronization point at $s_{s4}^*=1.0618m$. It is also shown that the amplitude of pressure perturbation generally increases with the lengthscale of the blowing-suction actuator increasing. In order to show the differences between cases 2 to 6 more clearly, two sections of Fig. 34 (a) are magnified as Figs. 34 (b) and 34 (c). Figure 34 (b) shows that the amplitude of pressure perturbation just after the blowing-suction actuator does increase with the lengthscale of the blowing-suction actuator increasing. After modulation, the amplitude of pressure perturbation does not necessarily increase with the lengthscale of the blowing-suction actuator increasing as shown in Fig. 34 (c). For example, the amplitude of pressure perturbation in case 5 is smaller than that in case 3 or 4 although the lengthscale of the blowing-suction actuator in case 5 is larger than that in case 3 or 4. In Figure 34 (d), similarly conclusions can be reached. Mode S is strongly excited for all eight cases, because blowing-suction actuators for all the cases are located

upstream of the corresponding synchronization point at $s^*_{s6} = 0.4719m$. However the amplitude of pressure perturbation does not necessarily increase with the lengthscale of the blowing-suction actuator increasing. For example, the amplitude of pressure perturbation in case 6 is the smallest although the lengthscale of blowing-suction actuator in case 6 is larger than that in case 1 to 5.

CONCLUSIONS

The receptivity of a Mach 8 flow over a sharp wedge with half-angle 5.3° to wall blowing-suction has been studied by numerical simulation as well as linear stability theory. The steady base flow is computed by solving the two-dimensional Navier-Stokes equations with a combination of a fifth-order shock-fitting method and a second-order TVD method. For unsteady flow simulations, periodic blowing-suction disturbances are superimposed to the steady base flow with the blowing-suction actuator on the wedge surface. Two different blowing-suction models are evaluated in this paper. It is found that the effect of the small instantaneous mass flux on receptivity is negligible, and the two blowing-suction models have same results for small-scale blowing-suction disturbances. Based on the results of numerical simulation and LST analysis, the receptivity process of the hypersonic boundary layer to a blowing-suction actuator is studied in detail. The effects of frequency, location, and lengthscale of the blowing-suction actuator on the receptivity are investigated.

The main conclusions of the current study are:

- Mode S is the dominant boundary-layer normal mode excited by the blowing-suction actuator. The receptivity of the hypersonic boundary layer to wall blowing-suction with different frequencies is quite different because the synchronization point in s^* coordinate depends on the dimensional frequency. With the dimensional frequency of disturbances increasing, the corresponding synchronization point moves upstream.

- The results show that the synchronization point plays an important role in the excitation of mode S by the blowing-suction actuator. Mode S is strongly excited when the blowing-suction actuator is located upstream of the corresponding synchronization point. On the other hand, when the blowing-suction actuator is downstream of the corresponding synchronization point, there is a significant decrease of the amplitude of the excited mode S. This decrease happens even when the blowing-suction actuator is still inside the unstable region of mode S.

- The lengthscale of blowing-suction actuator has a significant effect on receptivity of the hypersonic boundary layer to wall blowing-suction. However the amplitude of pressure perturbation does not necessarily increase with the lengthscale of the blowing-suction actuator increasing.

- The relationship between the location of the blowing-suction actuator and the synchronization point indicates: in order to control or delay the laminar-turbulent transition with wall blowing-suction, the blowing-suction actuator should be located upstream of the synchronization point of mode S and mode F.

ACKNOWLEDGEMENTS/DISCLAIMER

This work was sponsored by the Air Force Office of Scientific Research, USAF, under AFOSR Grant #FA9550-04-1-0029, monitored by Dr. John Schmisseur. The views and conclusions contained herein are those of the authors and should not be interpreted as necessarily representing the official policies or endorsements either expressed or implied, of the Air Force Office of Scientific Research or the U.S. Government.

References

[1] A. V. Fedorov and A. P. Khokhlov. Receptivity of Hypersonic Boundary Layer to Wall Disturbances. *Theoretical and Computational Fluid Dynamics*, 15:231–254, 2002.

[2] M. V. Morkovin. On the Many Faces of Transition. In C.S. Wells, editor, *Viscous Drag Reduction*, pages 1–31. Plenum, 1969.

[3] Th. Herbert. Secondary Instability of Boundary Layers. *Annual Review of Fluid Mechanics*, Vol. 20, pp. 487-526, 1988.

[4] M. E. Goldstein and L. S. Hultgren. Boundary-Layer Receptivity to Long-Wave Free-Stream Disturbances. *Annual Review of Fluid Mechanics*, Vol. 21, pp. 137-166 1989.

[5] L. M. Mack. Linear Stability Theory and the Problem of Supersonic Boundary-Layer Transition. *AIAA Journal*, Vol. 13, No. 3, pp. 278-289, 1975.

[6] M. Choudhari and C. L. Strett. Boundary Layer Receptivity Phenomena in Three-Dimensional and High-Speed Boundary Layers. *AIAA paper 90-5258*, 1990.

[7] M. Choudhari and C. L. Strett. Interaction of a High-Speed Boundary Layer with Unsteady Free-Stream Disturbances. *Transitional and Turbulent Compressible Flows*, L. D. Kral and T. A. Zang, editors, pp. 15-28, FED-Vol. 151, ASME, 1993.

[8] A. V. Fedorov and A. P. Khokhlov. Excitation of unstable modes in a supersonic boundary layer by

acoustic waves. *Fluid Dynamics (Translated From Russian)*, (4), pp.67-74, 1991.

[9] A. V. Fedorov and A. P. Khokhlov. Sensitivity of a supersonic boundary layer to acoustic disturbances. *Fluid Dynamics (Translated From Russian)*, (1), pp.40-47, 1992.

[10] A. V. Fedorov and V. Alexander. Laminar turbulent transition in a hypersonic boundary layer: Receptivity and instability pre-history. *Final report*, NASA-N97-29589, 1997.

[11] J. M. Kendall. Wind Tunnel Experiments Relating to Supersonic and Hypersonic Boundary-Layer Transition. *AIAA Journal*, Vol. 13, No. 3, pp. 290–299, 1975.

[12] A. A. Maslov and N. V. Seminov. Exitation of natural oscillations in a boundary layer. *Fluid Dynamics (Translated From Russian)*, (3):74–78, 1986.

[13] A. D. Kosinov N. V. Seminov and A. A. Maslov. An Experimental Study of Instability Disturbances Excitation by External Source in Supersonic Boundary Layer of a Blunted Plate. *Ineternational Conference on the Methods of Aerophysical Research (ICMAR' 98), Novosibirsk, Russia*, 1998.

[14] A. A. Maslov, A. N. Shiplyuk, A. Sidorenko, and D. Arnal. Leading-edge receptivity of a hypersonic boundary layer on a flat plate. *Jounral of Fluid Mechanics*, 426:73–94, 2001.

[15] M. R. Malik, R. S. Lin, and R. Sengupta. Computation of Hypersonic Boundary-Layer Response to External Disturbances. *AIAA Paper 99-0411*, January 1999.

[16] X. Zhong. Receptivity of hypersonic boundary layers to freestream disturbances. *AIAA paper 2000-0531*, January 2000.

[17] Y. Ma and X. Zhong. Receptivity of a supersonic boundary layer over a flat plate. Part 1:Wave Structures and Interactions. *Journal of Fluid Mechanics*, vol.488, pp.31-78, 2003.

[18] Y. Ma and X. Zhong. Receptivity of a supersonic boundary layer over a flat plate. Part 2:Receptivity to Freestream Sound. *Journal of Fluid Mechanics*, vol.488, pp.79-121, 2003.

[19] Y. Ma and X. Zhong. Receptivity of a supersonic boundary layer over a flat plate. Part 3. Effects of different types of free-stream disturbances. *Journal of Fluid Mechanics*, vol.532, pp.63-109, 2005.

[20] Y. Ma. Receptivity and Stability of Supersonic and Nonequilibrium Hypersonic Boundary Layers. *UCLA Ph.D Thesis*, 2003.

[21] I. V. Egorov, A. V. Fedorov, and V. G. Soudakov. Direct Numerical Simulation of Unstable Disturbances in Supersonic Boundary Layer. *AIAA paper 2004-0588*, January 2004.

[22] Y. Ma and X. Zhong. Receptivity to Freestream Disturbances of Mach 8 Flow over a Sharp Wedge. *AIAA paper 2003-0788*, 2003.

[23] X. Wang and X. Zhong. Receptivity of A Supersonic Boundary Layer over A Sharp Wedge to Wall Blowing/Suction. *AIAA paper 2004-0254*, January 2004.

[24] E. Forgoston and A. Tumin. Three-dimensional Wave Packet in a Hypersonic Boundary Layer. *AIAA paper 2005-0099*, January 2005.

[25] X. Zhong. Direct Numerical Simulation of Hypersonic Boundary-Layer Transition Over Blunt Leading Edges, Part I: New Numerical Methods and Validation (Invited). *AIAA paper 97-0755, 35th AIAA Aerospace Sciences Meeting and Exhibit, January 6-9, Reno, Nevada*, 1997.

[26] X. Zhong. High-Order Finite-Difference Schemes for Numerical Simulation of Hypersonic Boundary-Layer Transition. *Journal of Computational Physics*, Vol. 144, pp. 662-709, 1998.

[27] X. Zhong. Additive Semi-Implicit Runge-Kutta Schemes for Computing High-Speed Nonequilibrium Reactive Flows. *Journal of Computational Physics*, 128:19–31, 1996.

[28] J. J. Yoh and X. Zhong. Low-storage semi-implicit runge-kutta methods for reactive flow computations. *AIAA paper 98-0130*, January 1998.

[29] X. Zhong and T. Lee. Nonequilibrium real-gas effects on disturbance/bow shock interaction in hypersonic flow past a cylinder. *AIAA paper 96-1856*, January 1996.

[30] W. Eibler and H. Bestek. Spatial Numerical Simulations of Linear and Weakly Nonlinear Instabilities in Supersonic Boundary Layers. *Theoretical and Computational Fluid Dynamics*, 8:219–235, 1996.

[31] Y. Ma and X. Zhong. Receptivity to Freestream Disturbances of Mach 4.5 Flow over A Flat Plate. *AIAA Paper 2002-0140*, January 2002.

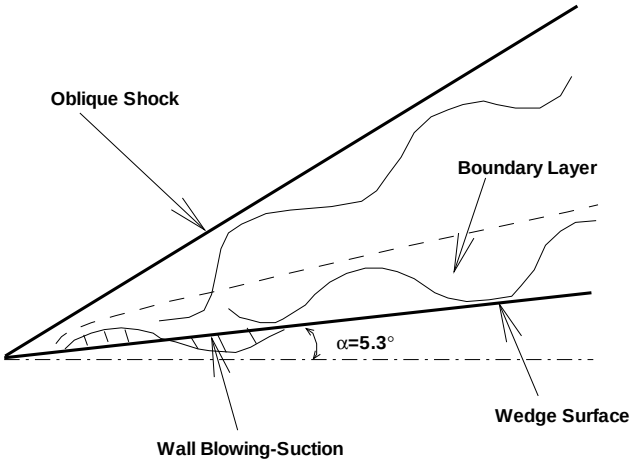

Figure 1: A schematic of the receptivity of a hypersonic boundary layer over a sharp wedge to wall blowing-suction.

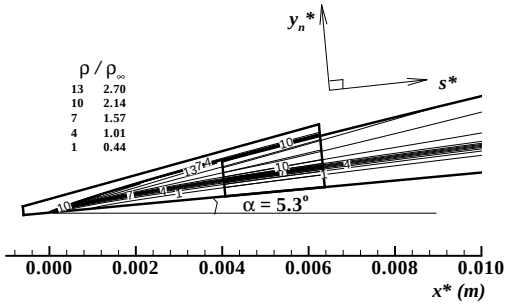

Figure 2: Contours of density near the leading edge for steady base flow (Ma and Zhong[22]).

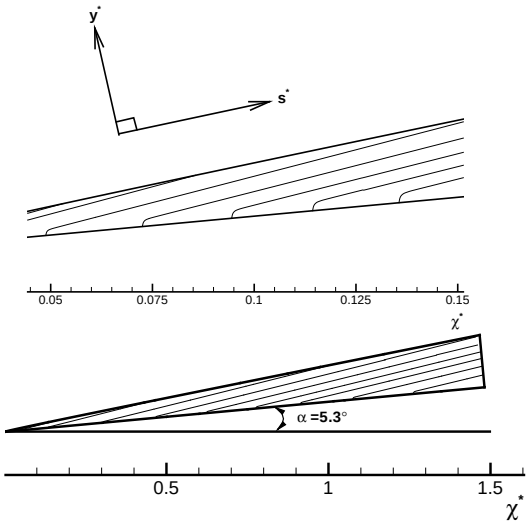

Figure 3: Contours of pressure for steady base flow ($M_\infty = 8$).

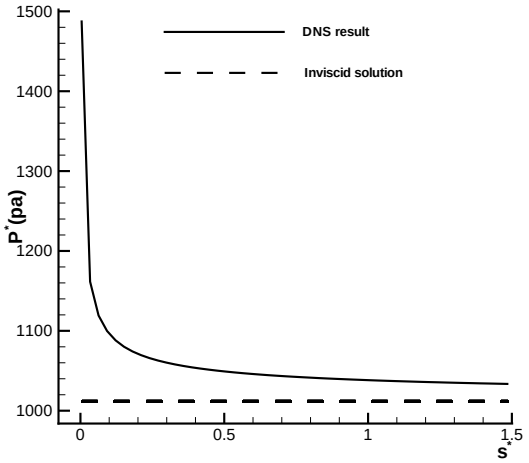

Figure 4: Comparison of pressure distributions along the wedge surface of numerical simulation result and theoretical inviscid solution.

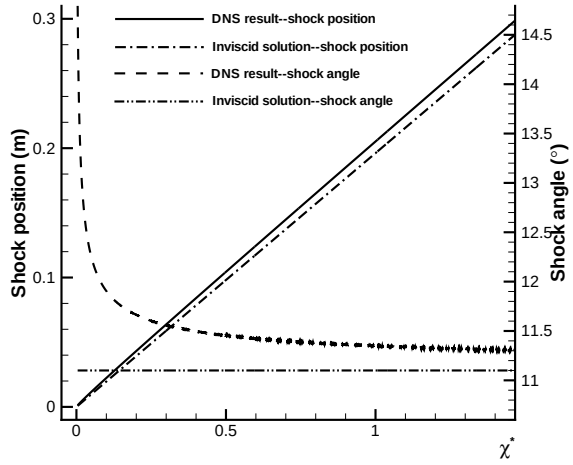

Figure 5: Comparisons of shock positions and shock angles of numerical simulation result and theoretical inviscid solution respectively.

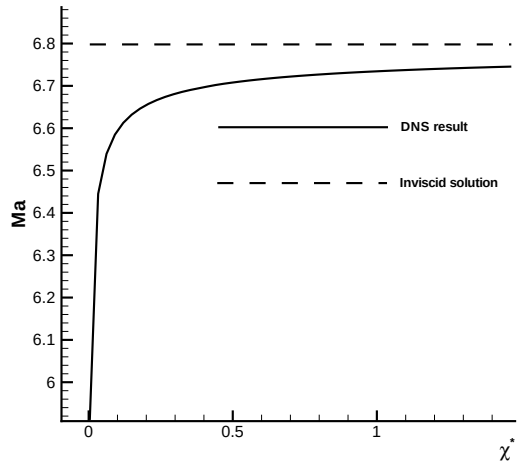

Figure 6: Comparison of Mach number distributions behind the shock of numerical simulation result and theoretical inviscid solution.

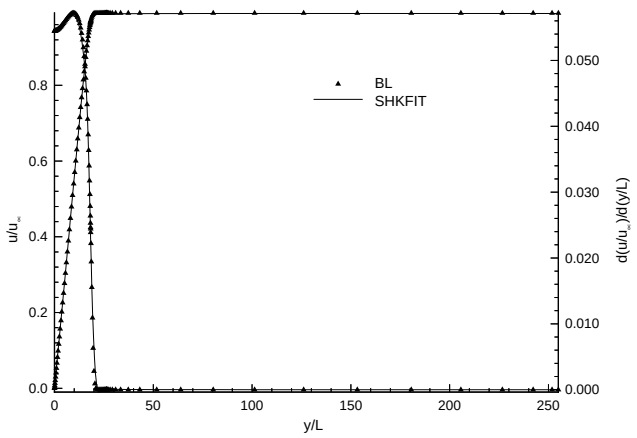

Figure 7: Comparisons of stream-wise velocity and its first-order derivative between shock-fitting simulation and self-similar boundary-layer solution ($s^* = 0.62784$ m, $R = 2264.13$).

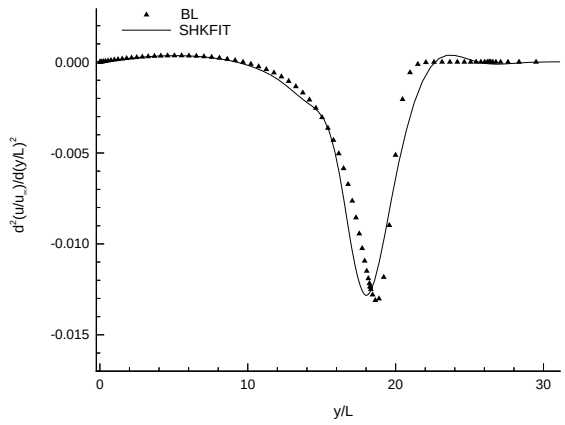

Figure 8: Comparison of the second-order derivative of streamwise velocity between shock-fitting simulation and self-similar boundary-layer solution ($s^* = 0.62784$ m, $R = 2264.13$).

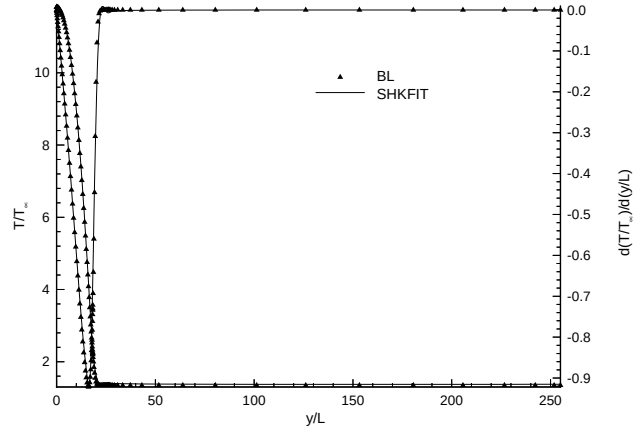

Figure 9: Comparisons of temperature and its first-order derivative between shock-fitting simulation and self-similar boundary-layer solution ($s^* = 0.62784$ m, $R = 2264.13$).

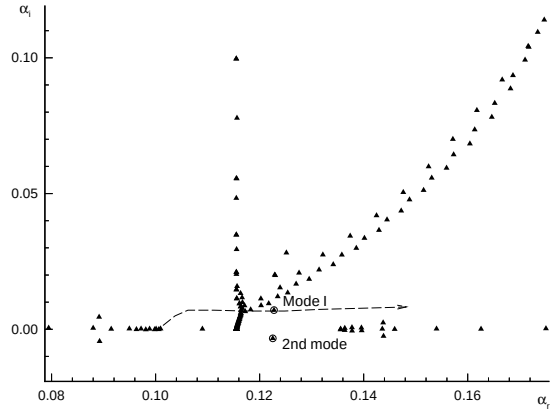

Figure 10: Eigenvalue spectra of boundary-layer modes for the disturbance with the frequency $f_6^* = 89.52$ kHz at $s^* = 0.48036$ m (In the present paper, Mode I is termed as mode F, while 2nd mode is termed as mode S).

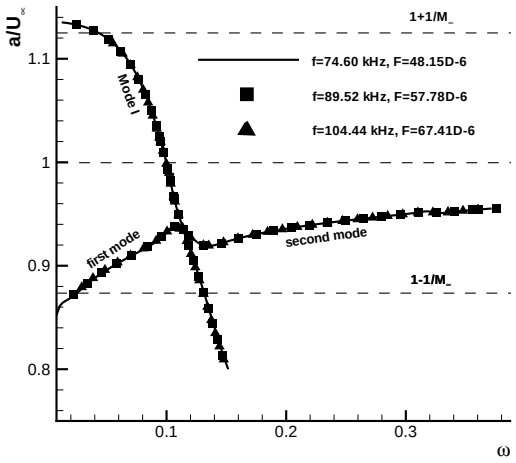

Figure 11: Comparison of non-dimensional phase velocities of boundary-layer normal modes with different frequencies (In the present paper, Mode I is termed as mode F, while first Mack mode and second Mack mode are termed as mode S).

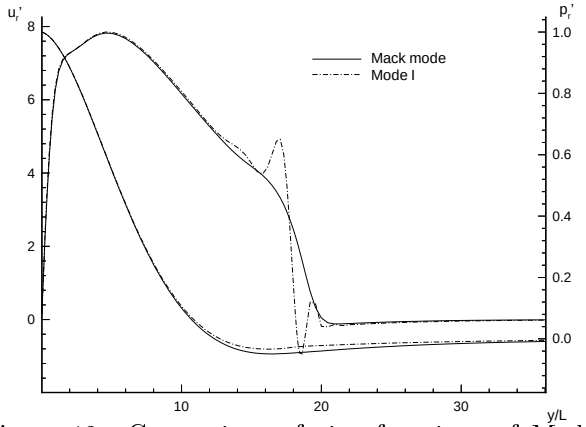

Figure 12: Comparison of eigenfunctions of Mode I (mode F) and Mack mode (mode S) at the synchronization point.

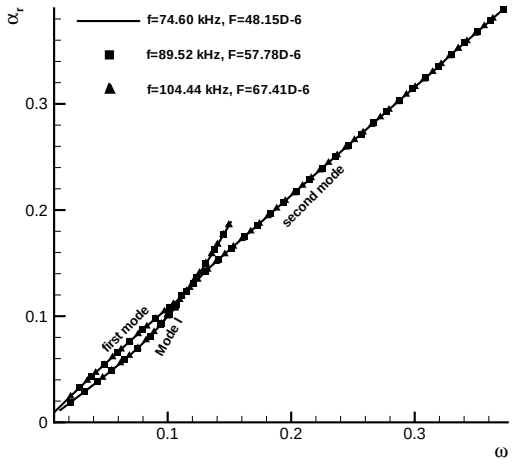

Figure 13: Comparison of wave numbers of boundary-layer modes with different frequencies (In the present paper, Mode I is termed as mode F, while first Mack mode and second Mack mode are termed as mode S).

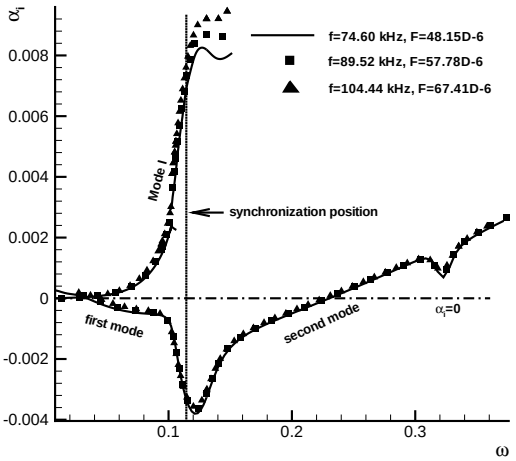

Figure 14: Comparison of growth rates of boundary-layer modes with different frequencies (In the present paper, Mode I is termed as mode F, while first Mack mode and second Mack mode are termed as mode S).

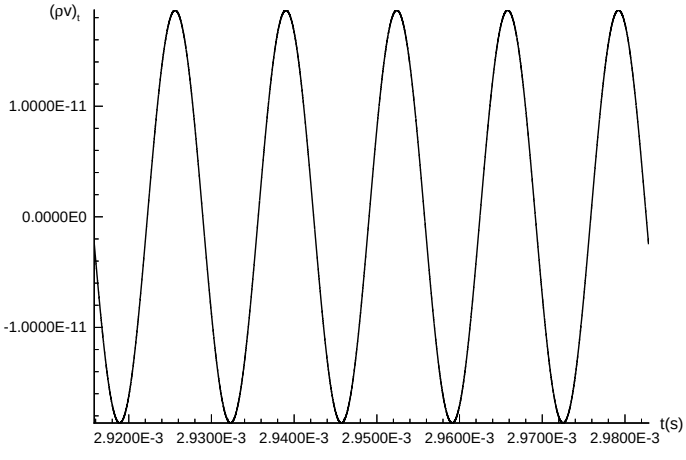

Figure 15: Evolution of mass flux introduced to the boundary layer by the normal velocity blowing-suction disturbance during one period of the base frequency.

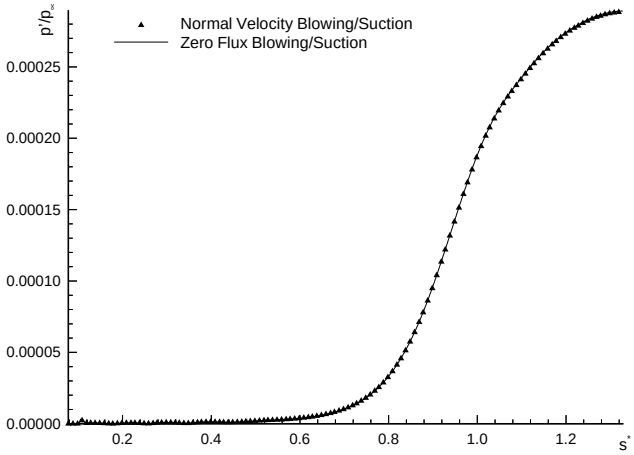

Figure 16: Comparison of non-dimensional perturbation amplitudes along the wedge surface for two kinds of blowing-suction disturbances.

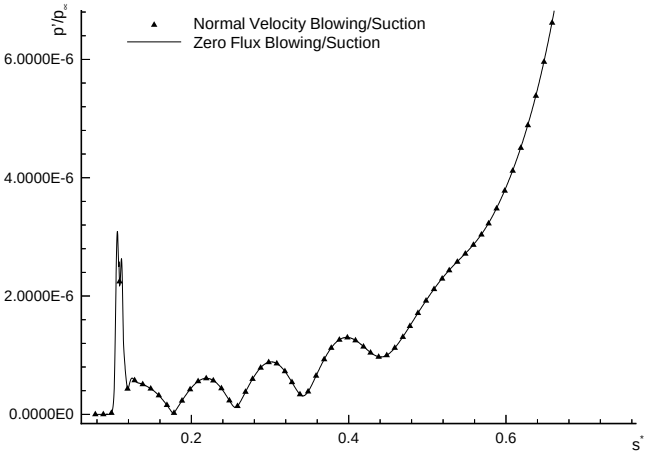

Figure 17: A blow-up of figure 16 on the comparison of upstream perturbation amplitudes along the wedge surface for two kinds of blowing-suction disturbances.

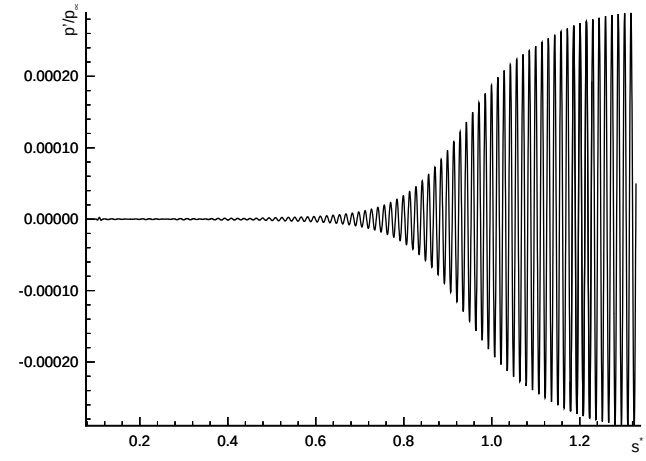

Figure 18: Distribution of instantaneous pressure perturbation along the wedge surface ($F_5 = 48.15 \times 10^{-6}$, $f_5^* = 74.60$ kHz).

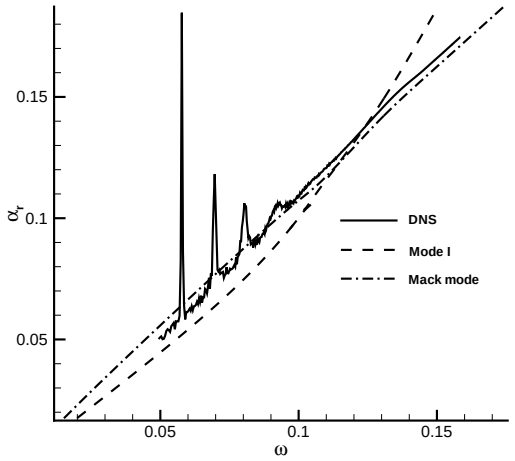

Figure 19: Comparison of the wave number α_r solved by numerical simulation with those of Mode I (mode F) and the Mack mode (mode S) obtained by LST ($f_5^* = 74.60$ kHz).

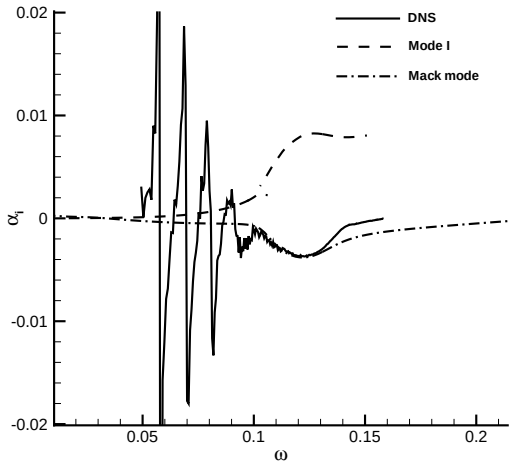

Figure 20: Comparison of the growth rate α_i solved by numerical simulation with those of Mode I (mode F) and the Mack mode (mode S) obtained by LST ($f_5^* = 74.60$ kHz).

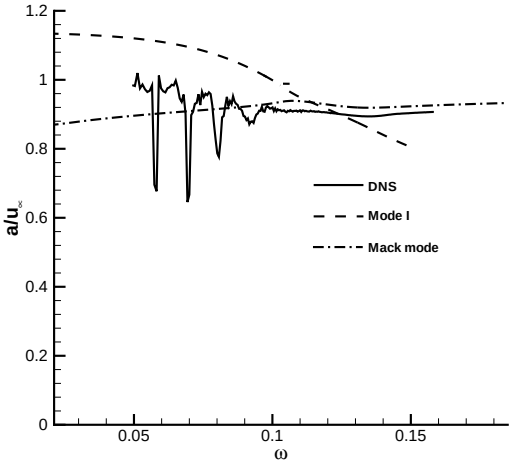

Figure 21: Comparison of the non-dimensional phase velocity a/u_∞ solved by numerical simulation with those of Mode I (mode F) and the Mack mode (mode S) obtained by LST ($f_5^* = 74.60$ kHz).

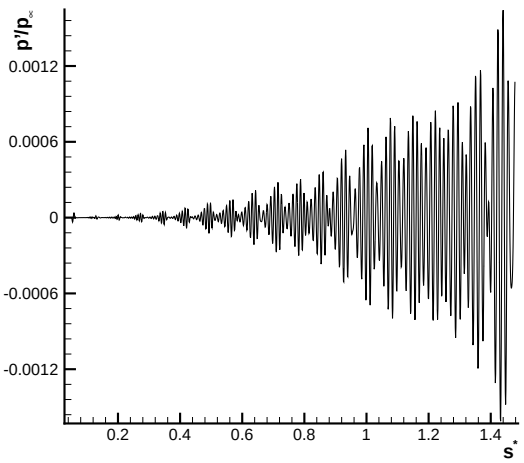

Figure 22: Distribution of instantaneous pressure perturbation along the wedge surface for the fifteen-frequency blowing-suction actuator in (0.05184 m, 0.06384 m).

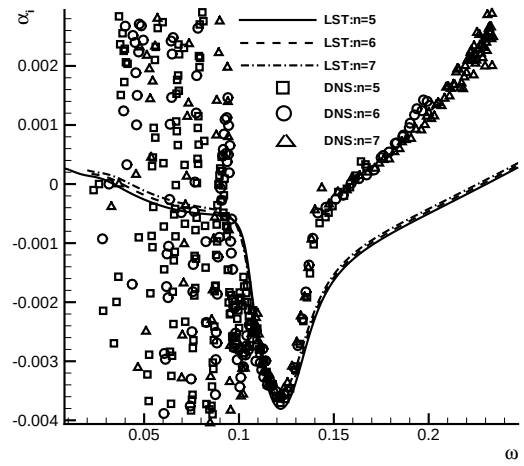

Figure 23: Comparison of numerical growth rates and LST growth rates of perturbations with frequencies f_5^*, f_6^*, and f_7^* (α_i vs ω).

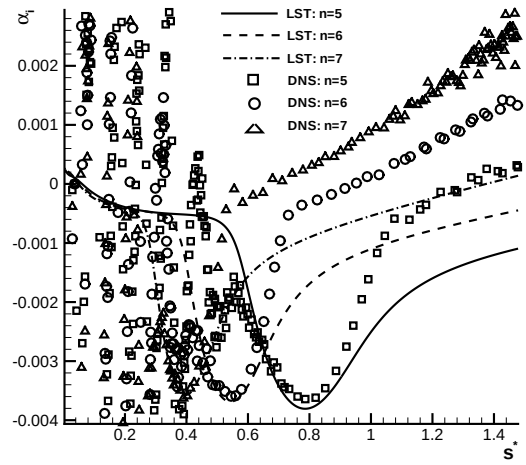

Figure 24: Comparison of numerical growth rates and LST growth rates of perturbations with frequencies f_5^*, f_6^*, and f_7^* (α_i vs s^*).

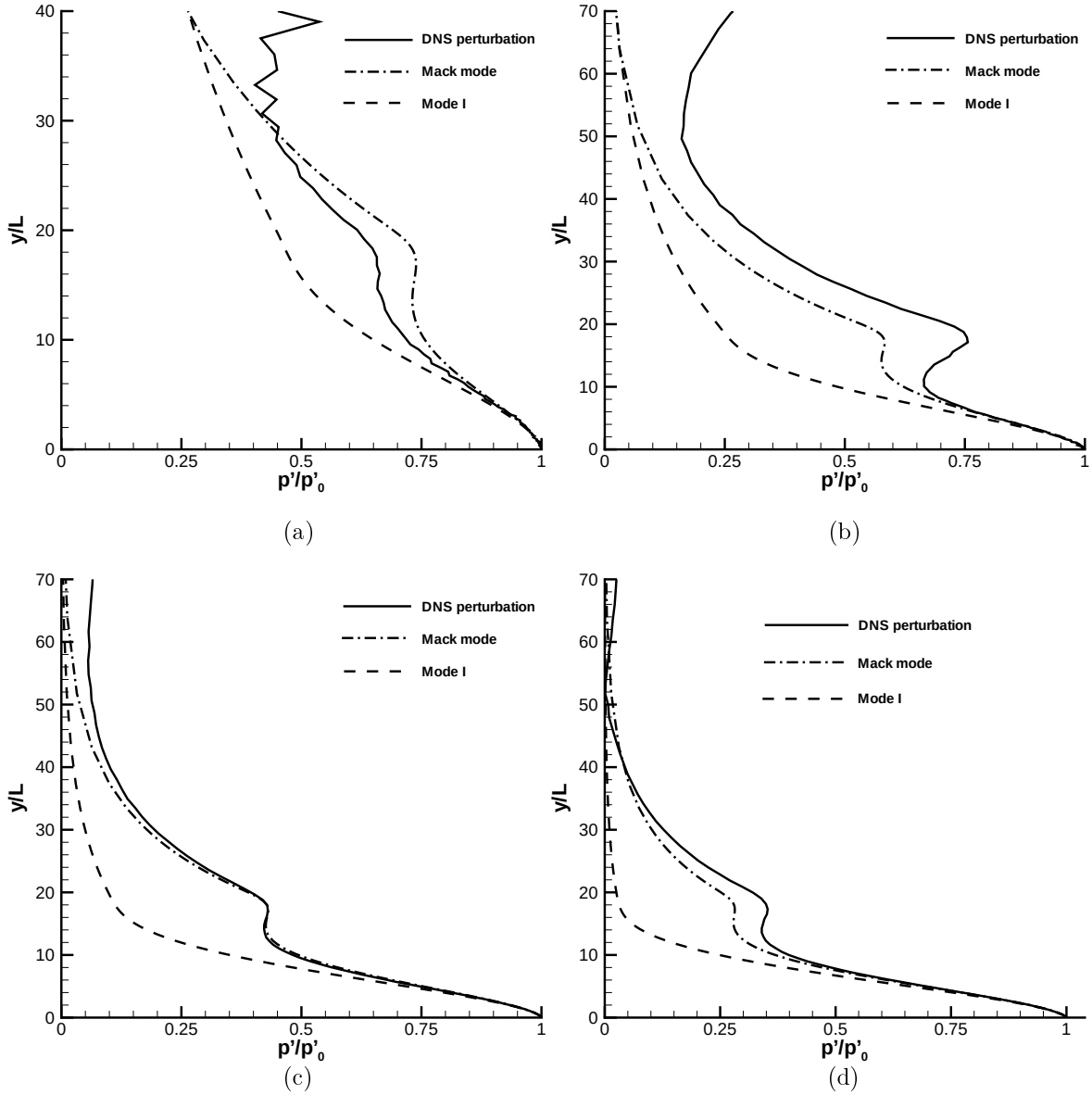

Figure 25: Comparison of the eigenfunctions of Mode I (mode F) and Mack mode (mode S) with the instantaneous pressure perturbation (frequency f_5^*) from numerical simulation at different locations: (a) $\omega = 0.055945$ ($s^* = 0.16534$ m); (b) $\omega = 0.070872$ ($s^* = 0.26534$ m); (c) $\omega = 0.083161$ ($s^* = 0.36534$ m); (d) $\omega = 0.093855$ ($s^* = 0.46534$ m).

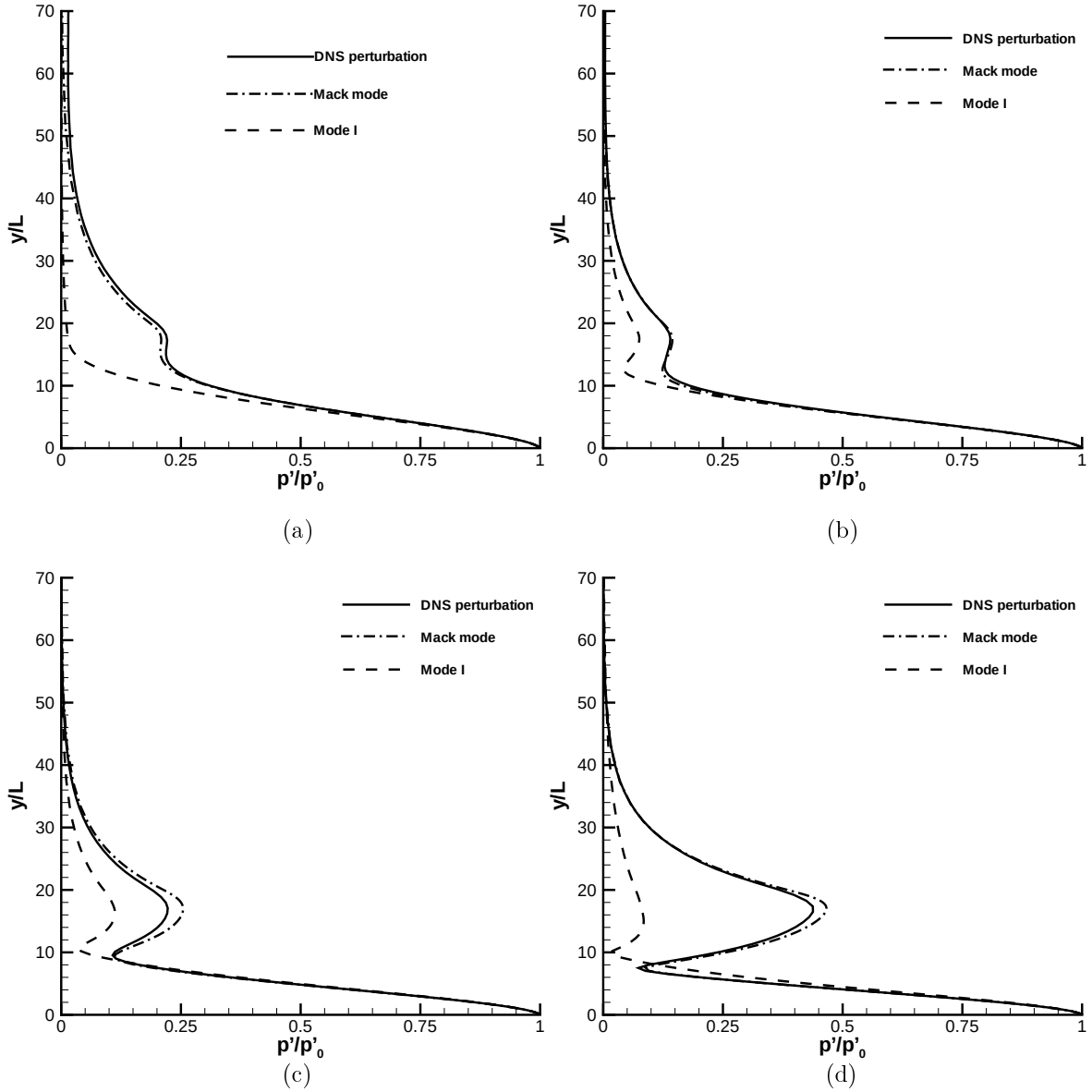

Figure 26: Comparison of the eigenfunctions of Mode I (mode F) and Mack mode (mode S) with the instantaneous pressure perturbation (frequency f_5^*) from numerical simulation at different locations: (a) $\omega = 0.098769$ ($s^* = 0.51534$ m); (b) $\omega = 0.11223$ ($s^* = 0.66534$ m); (c) $\omega = 0.12799$ ($s^* = 0.86534$ m); (d) $\omega = 0.14530$ ($s^* = 1.11534$ m).

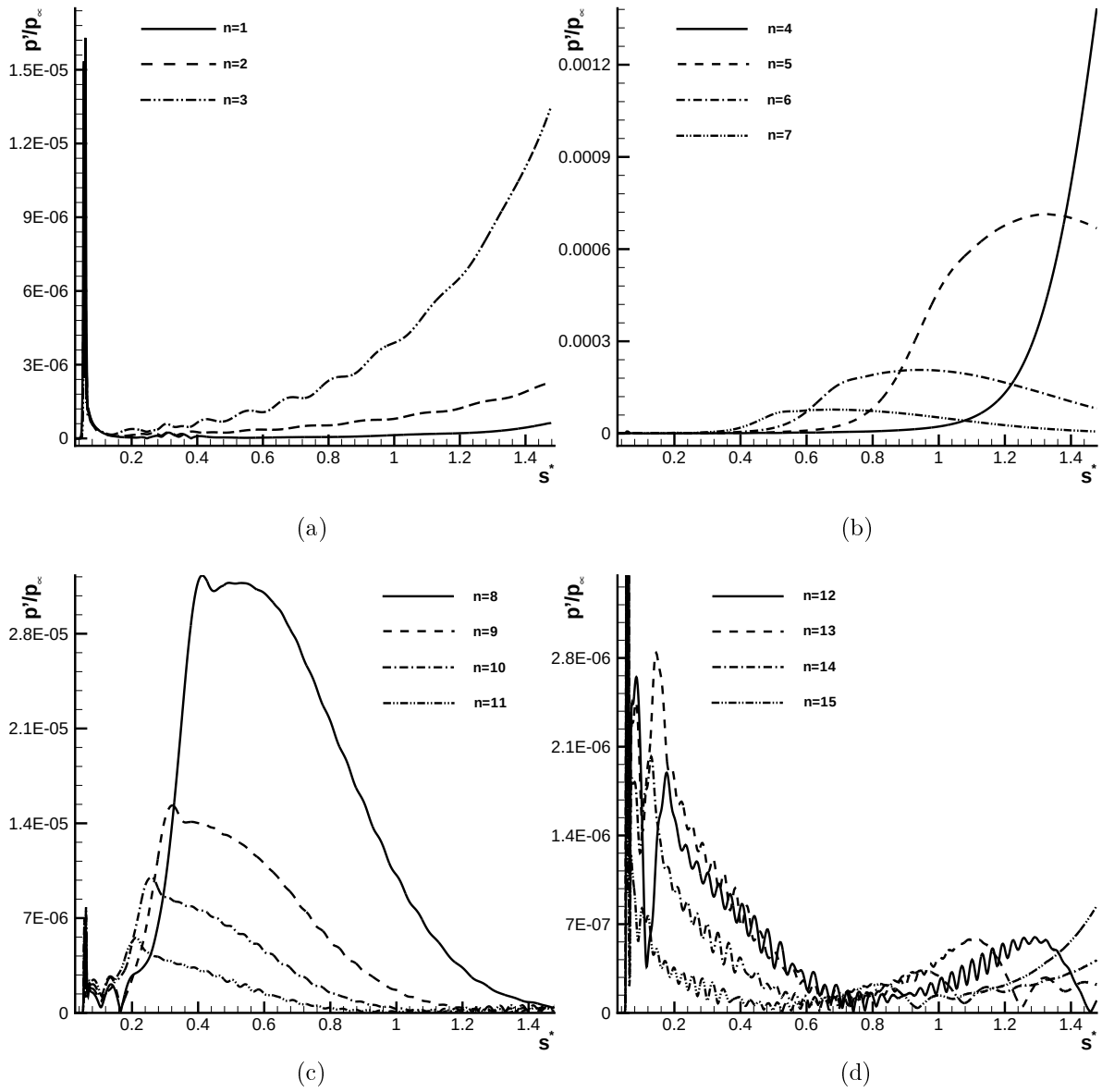

Figure 27: Comparisons of perturbation amplitudes along the wedge surface with different frequencies for the case that fifteen-frequency blowing-suction disturbances are enforced on the wedge surface from $s_i^* = 0.05184$ m to $s_e^* = 0.06384$ m.

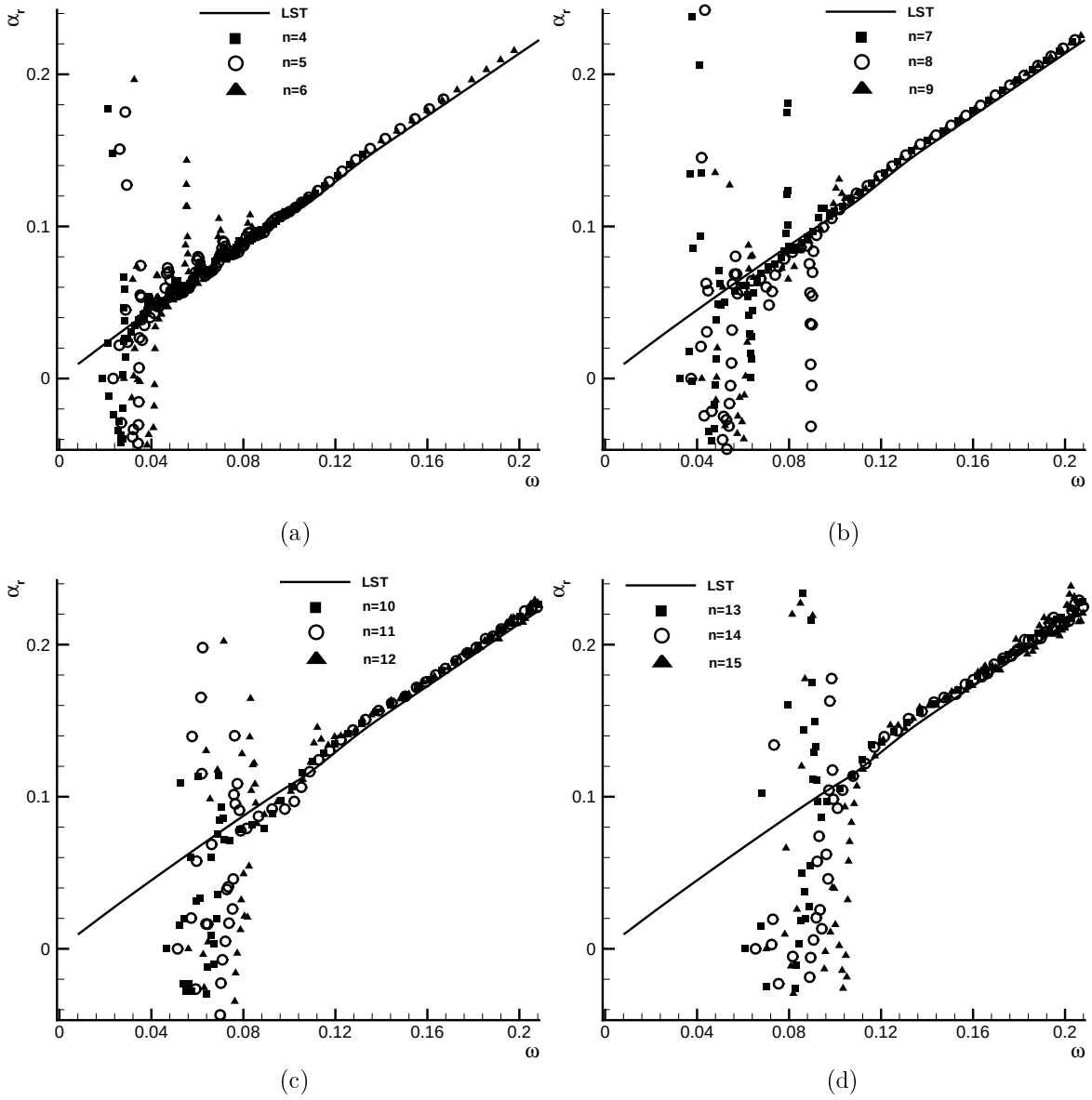

Figure 28: Comparisons of numerical wave numbers and the LST wave number of perturbations with frequency f_n^* (n from 4 to 15) for the case that fifteen-frequency blowing-suction disturbances are enforced on the wedge surface from $s_i^* = 0.05184$ m to $s_e^* = 0.06384$ m.

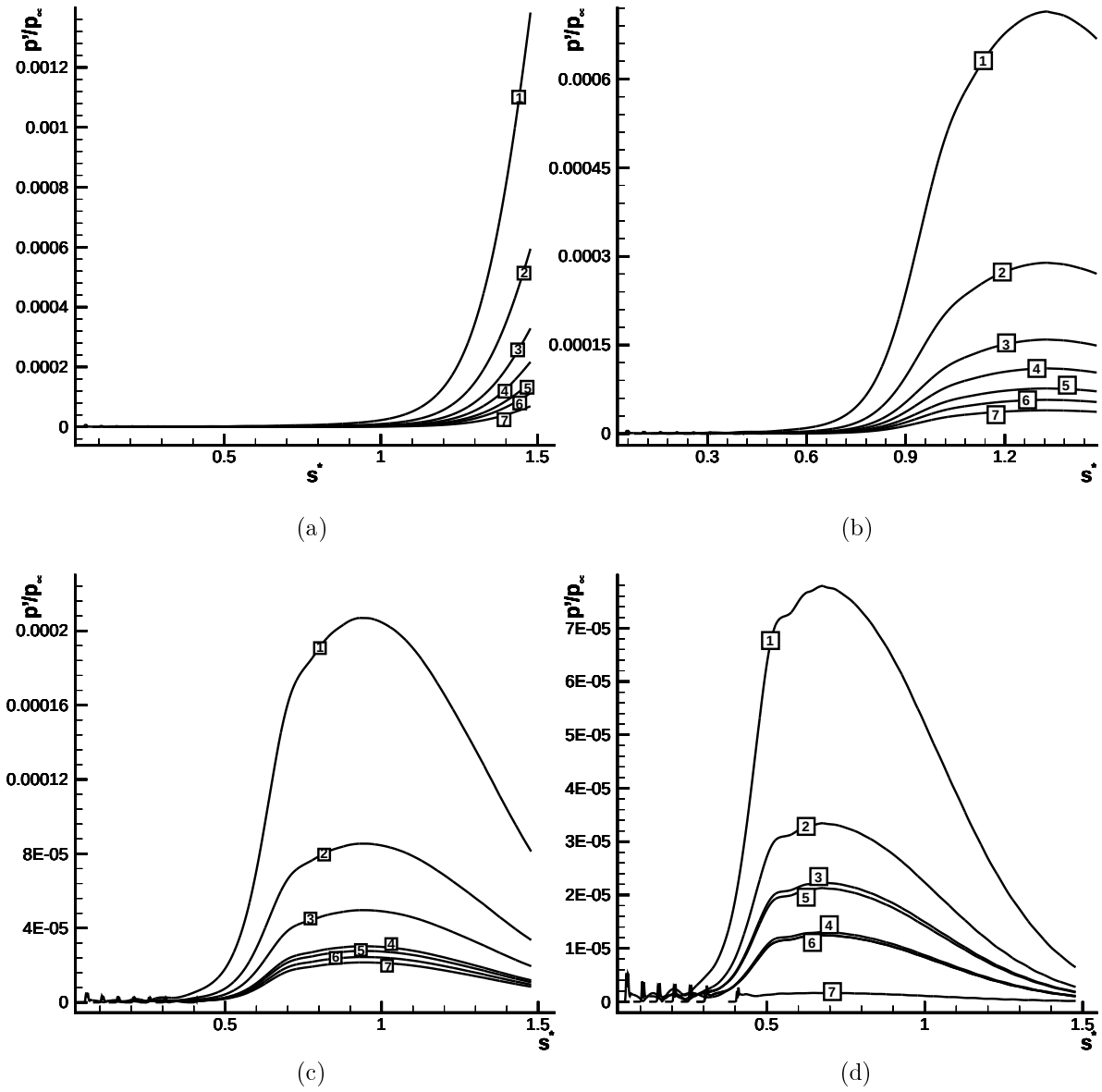

Figure 29: Comparisons of perturbation amplitudes with a same frequeny for cases that blowing-suction disturbances are enforced on the wedge surface at different locations: (a) $f_4^* = 59.68$ kHz; (b) $f_5^* = 74.60$ kHz; (c) $f_6^* = 89.52$ kHz; (d) $f_7^* = 104.44$ kHz.

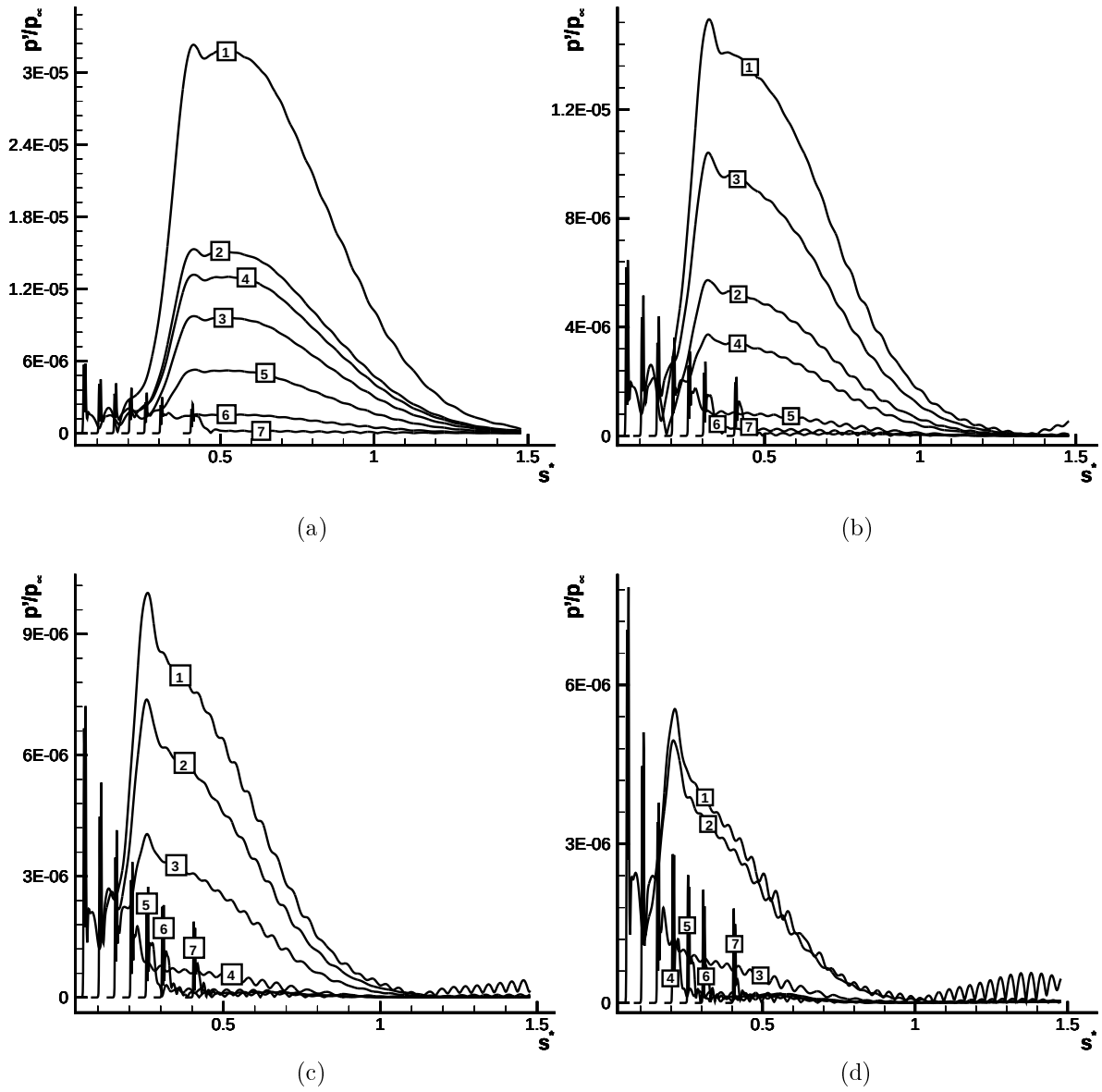

Figure 30: Comparisons of perturbation amplitudes with a same frequeny for cases that blowing-suction disturbances are enforced on the wedge surface at different locations: (a) $f_8^* = 119.36$ kHz; (b) $f_9^* = 134.28$ kHz; (c) $f_{10}^* = 149.20$ kHz; (d) $f_{11}^* = 164.12$ kHz.

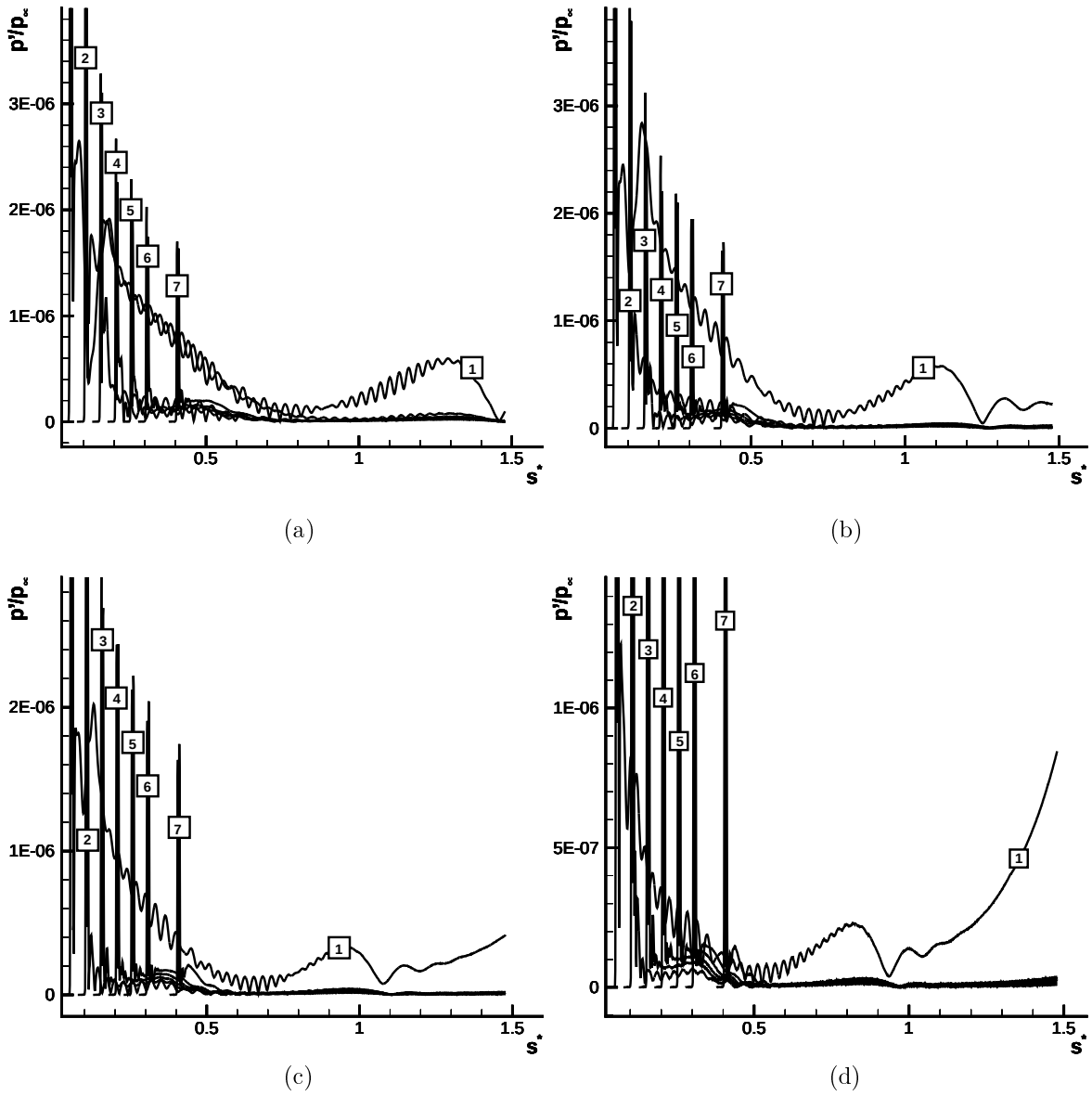

Figure 31: Comparisons of perturbation amplitudes with a same frequeny for cases that blowing-suction disturbances are enforced on the wedge surface at different locations: (a) $f_{12}^* = 179.04$ kHz; (b) $f_{13}^* = 193.96$ kHz; (c) $f_{14}^* = 208.88$ kHz; (d) $f_{15}^* = 223.80$ kHz.

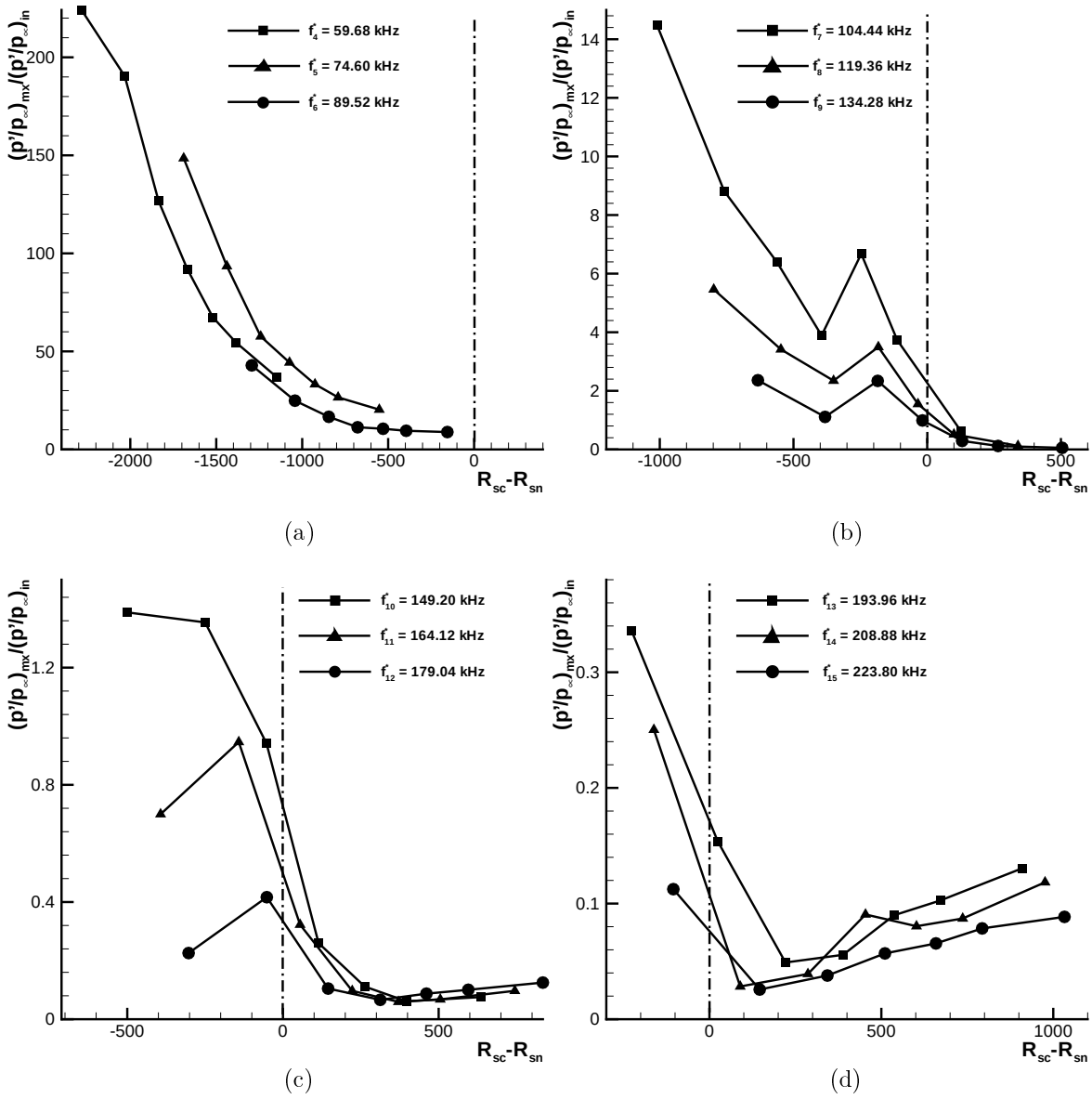

Figure 32: Comparisons of response coefficients of pressure perturbations with a same frequency for cases that the blowing-suction actuator are located on the wedge surface at different locations: (a) f_n^* with n from 4 to 6; (b) f_n^* with n from 7 to 9; (c) f_n^* with n from 10 to 12; (d) f_n^* with n from 13 to 15.

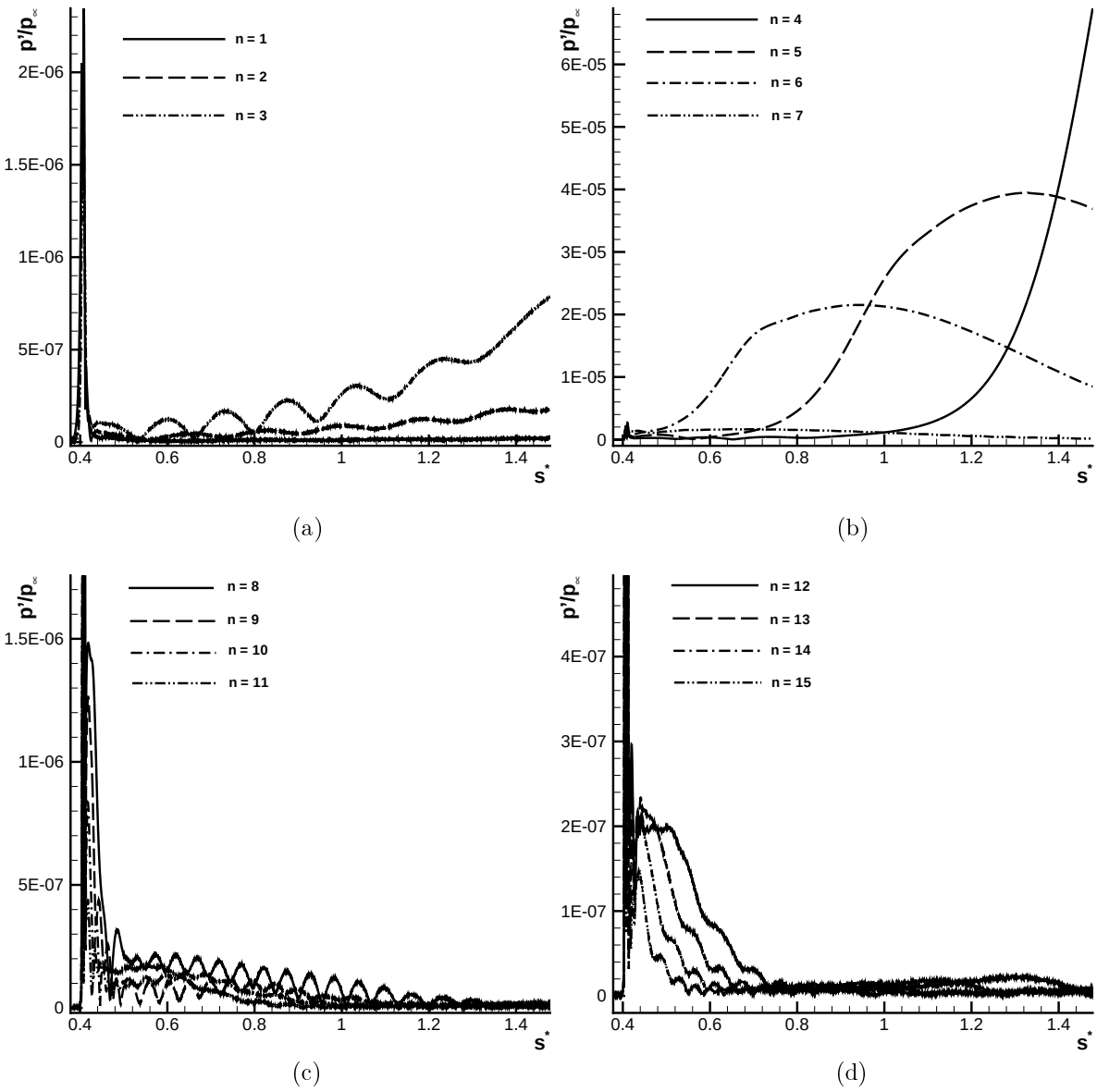

Figure 33: Comparisons of perturbation amplitudes along the wedge surface with different frequencies for the case that the fifteen-frequency blowing-suction actuator are located on the wedge surface from $s_i^* = 0.40184$ m to $s_e^* = 0.41384$ m.

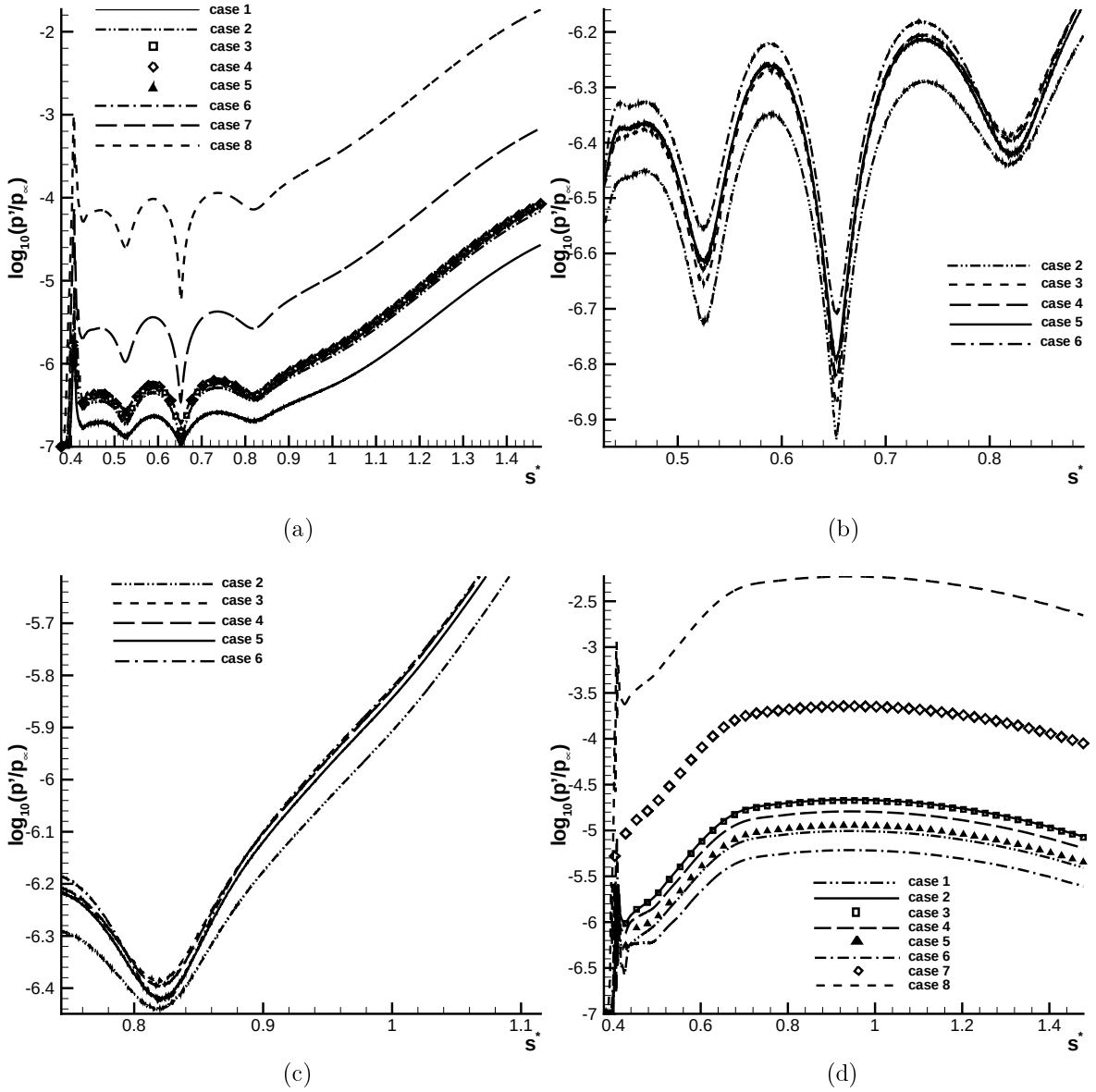

Figure 34: Comparisons of perturbation amplitudes with a same frequeny for cases that blowing-suction disturbances are introduced by blowing-suction actuators with different lengthscales at the same location on the wedge surface: (a) $f_4^* = 59.68$ kHz; (b) $f_4^* = 59.68$ kHz (upstream magnification); (c) $f_4^* = 59.68$ kHz (downstream magnification); (d) $f_6^* = 89.52$ kHz.